PHILOSOPHICAL TRANSACTIONS OF THE ROYAL SOCIETY B BIOLOGICAL SCIENCES

Graded-Index Optics are Matched to Optical Geometry in the Superposition Eyes of Scarab Beetles

P. McIntyre and S. Caveney

Phil. Trans. R. Soc. Lond. B 1985 **311**, 237-269
doi: 10.1098/rstb.1985.0153

Phil. Trans. R. Soc. Lond. B **311**, 237–269 (1985) [237]
Printed in Great Britain

GRADED-INDEX OPTICS ARE MATCHED TO OPTICAL GEOMETRY IN THE SUPERPOSITION EYES OF SCARAB BEETLES

By P. McINTYRE[1,3] and S. CAVENEY[2,3]

[1]*Department of Mathematics, Faculty of Military Studies, University of New South Wales, Duntroon, ACT* 2600 *Australia*
[2]*Department of Zoology, University of Western Ontario, London, Ontario, Canada N6A 5B7*
[3]*Department of Neurobiology, Research School of Biological Sciences, Australian National University, Canberra, ACT* 2601 *Australia*

(*Communicated by M. F. Land, F.R.S.* – *Received* 20 *September* 1984)

[Plates 1–4]

CONTENTS

Detailed measurements were made of the gradients of refractive index (g.r.i.) and relevant optical properties of the lens components in the ventral superposition eyes of three crepuscular species of the dung-beetle genus *Onitis* (Scarabaeinae). Each ommatidial lens has two components, a corneal facet and a crystalline cone; in both of these, the gradients provide a significant proportion of the refractive power. The spatial relationship between the lenses and the retina (optical geometry) was also determined. A computer ray-trace model based on these data was used to analyse the optical properties of the lenses and of the eye as a whole. Ray traces were done in two and three dimensions.

The ommatidial lenses in all three species are afocal g.r.i. telescopes of low angular magnification. Parallel incident rays emerge approximately parallel for all angles of incidence up to the maximum. The superposition image of a distant point source is a small patch of light about the size of a rhabdom.

There are obvious differences in the lens properties of the three species, most significantly in the shape of the refractive-index gradients in the crystalline cone, in the extent of the g.r.i. region in the two lens components and in the front-surface curvature of the corneal facet lens. These give rise to different angular magnifications M of the ommatidial lenses, the values for the three species being 1.7, 1.3, 1.0. This variation in M is matched by a variation in optical geometry, most evident in the different clear-zone widths. As a result, the level of the best superposition image lies close to the retina in the model eyes of all three species. The angular magnification also sets the maximum aperture or pupil of the eye and hence the brightness of the image on the retina. The smaller M, the larger the aperture and the brighter the image. By adopting a suitable value for M and the appropriate eye geometry, an eye can set image brightness and hence sensitivity within a certain range.

Differences in the eye design are related to when the beetles fly at dusk. Flight experiments comparing two of the species show that the species with the higher value for M and corresponding lower sensitivity, initiates and terminates its flight earlier in the dusk than the other species with 2.8 times the sensitivity.

1. INTRODUCTION

The formation of superposition images in clear-zone compound eyes requires particular optics in the refracting lens elements of each ommatidium (Exner 1891; Kunze 1979). For a good superposition image to fall on the retina: the spread of light leaving the proximal tip of each crystalline cone must be narrow; the lens elements must be precisely aligned; the angular magnification M of the individual ommatidial lenses (ratio of the beam emergent angle to the incident angle) must be matched to the geometry of the eye. In an eye with spherical symmetry, M must be approximately constant for all angles of incidence. The structure of the compound eye in different arthropods, however, suggests that M can vary considerably between species.

Parallel rays entering a corneal facet are brought to a focus within the crystalline cone by the lens system, and emerge from the proximal tip of the cone approximately parallel again. This is accomplished in many beetles by the presence of graded-refractive-index (g.r.i.) lenses in both the cornea and crystalline cones (Caveney & McIntyre 1981). In the few arthropod eyes in which these refractive-index gradients have been measured, they vary approximately

parabolically with distance from the optical axis of the lens (Hausen 1973; Vogt 1974; Land & Burton 1979). Following the work of Fletcher *et al.* (1954), it has been assumed that a sech gradient (which is approximately parabolic) is optimal for focussing light with a g.r.i. lens. However, as pointed out by Marchand (1982), a sech gradient is not necessarily optimal if the lens also has refracting surfaces, and does not bring skew rays to a sharp focus. Non-parabolic gradients were found in the eye of a beetle, *Anoplognathus* (Caveney & McIntyre 1981).

In this paper we report on the optical properties of the ommatidial lenses and on how they are matched to the geometry of the compound eye in three species of dung beetle. The width of the clear zone (relative to eye size) was found to be quite different in the different species, yet the optics of the lenses in each case are such that a good superposition image falls upon the retina. We chose to study the problem in dung beetles because closely related species fly at different times of the day, and it should be possible to distinguish features in eye structure that are physiological adaptations to flight at different light intensities from those that result from different ancestry. Caveney & McIntyre (1981) have already noted that a strong outer-surface curvature to the corneal facet lenses and the presence of screening pigment between these lenses are qualitative features associated with diurnal beetles. Here we examine quantitatively the optical properties of the eye as a whole and the differences between the eyes of the three species in relation to their time of flight.

2. Materials and methods

(*a*) *Beetles used*

Three introduced species of the dung-beetle genus *Onitis* (Scarabaeinae) were used in this study. *O. aygulus* F. and *O. westermanni* Lansberge were obtained from laboratory stocks kept at the Commonwealth Scientific and Industrial Research Organization in Canberra. *O. alexis* Klug was collected from pastures at Araluen and Moruya, New South Wales.

(*b*) *Histology*

Beetles were rapidly decapitated, the heads dropped in a cold fixative solution consisting of 25 g l^{-1} glutaraldehyde and 0.14 M sucrose in 0.1 M cacodylate buffer at pH 7.2, and left overnight at 4 °C. Following post-fixation in 10 g l^{-1} OsO_4 in the same buffer solution, the heads were bisected gently (to prevent distortion of the eye tissue), dehydrated through an alcohol series and embedded in Araldite. Because of the large size of the heads, the plastic was allowed to infiltrate the tissue overnight at room temperature under vacuum before polymerization at 60 °C. Thin sections were cut at a thickness of 1–2 μm and stained with toluidine blue for light microscopy.

(*c*) *Optics*

Refractive-index measurements were made with a Zeiss double-beam interference microscope at 100× objective magnification. Corneal refractive-index gradients were determined from freshly sliced corneal sections by the double-immersion procedure given in Caveney & McIntyre (1981).

Refractive-index gradients within the crystalline cones were derived from retardation measurements across intact cones immersed in a physiological saline ($n = 1.336$). The retardation measurements were processed as in Nilsson *et al.* (1983) to give a curve of $n(r)$ versus

radial position r for each region of each cone measured. The radial positions were then normalized by dividing by the radius of the cone region. Mean curves were calculated from these normalized curves.

The focal lengths of the corneal facets were determined from isolated corneal slices as outlined in Caveney & McIntyre (1981).

(*d*) *Measurement of optical geometry*

The spatial relationship between the lens elements and the retina in the compound eye was determined by light microscopical examination of toluidine-blue-stained sections of plastic-embedded material. An eyepiece graticule inscribed with a set of calibrated concentric circles was used to measure the radii of curvature of the surfaces along which the lenses and the photoreceptor cells are arranged.

A superposition eye with perfect spherical symmetry has the various components of the eye arranged as a series of concentric shells. The true curvatures are only obtained from those sections that pass through the centre of curvature of the eye. Sections that do not will yield measured radii of curvature less than the true values. Fortunately, the radially elongated nature of several eye structures, such as the retinular-cell extensions and the rhabdom in each ommatidium, made it easy to determine when the section was along an eye radius.

The eyes of the beetles studied in this paper, however, deviated from perfect spherical symmetry. The crystalline cones were aligned along a spherical curvature. The rhabdom layer, too, is spherical, but is not concentric with the crystalline cones, and is flatter than it would be if the eye were spherically symmetrical. Furthermore, the curvatures of the corneal surface and of the crystalline-cone layer were tighter at the margin of the eye than over its general surface. Consequently, only the central region of the eye (typically more than three-quarters of the distance between the eye margins) was used in the measurements. The heads were positioned in the plastic blocks so that the plane of the section passed through the dorsal and ventral margins of the eye, and the eye was sectioned radially in this region.

(*e*) *Flight trials*

The flight activity of beetles was tested in a rectangular flight chamber 2 m long × 0.9 m wide × 0.3 m high. This chamber, originally designed to extract beetles from fresh dung (Houston *et al.* 1982) was light-tight except for a window (covered with wire mesh) at one end. The floor in the chamber immediately beneath the window was open and constructed to allow three plastic containers to be inserted to fill the space. The flight chamber was placed in a heated greenhouse, with the window end projecting out of the greenhouse and exposed to natural light. Beetles to be flown were placed in a 5 cm deep layer of soil at the dark end of the chamber several hours before the experiment began. The soil and air temperatures in the chamber were measured with thermistor probes connected to a Grant recorder. Light levels were measured with a radiometer (International Light Model IL700), with the silicon detector (SEE 100W) placed at the window end of the chamber to measure the intensity of the natural light falling on the window. The beetles were flown on the evenings of 14 and 15 April, 1982. At dusk, the beetles emerged from the soil, flew towards the window of the chamber, hit the mesh, and dropped through funnels into water in the plastic containers. At 10 min intervals the containers were removed, replaced with new ones, and the beetles in them counted.

PHILOSOPHICAL TRANSACTIONS OF THE ROYAL SOCIETY B BIOLOGICAL SCIENCES

3. Results

(a) *General features of the eye*

The compound eye of *Onitis*, as in most dung beetles, is divided completely into a large ventral region and a smaller dorsal region by a cuticular ridge, or canthus (Caveney & McIntyre 1981). The field of view of the dorsal eye is restricted to upwards, but the ventral eye has a less restricted view.

The data in this paper are from the ventral eyes of three species of *Onitis*; *O. aygulus*, *O. alexis* and *O. westermanni*. In all three species the corneal surface is sculpted with an hexagonal array of facets. *O. aygulus* has a weaker facet curvature than the other two species (table 1, compare figure 2 with figures 5 and 7, plates 1–3). The facet lens, hexagonal at the surface of the eye, extends inwards as a slightly tapered cylinder. In *O. westermanni* the proximal tip of the corneal lens is hemispherical in shape (figure 7), but in *O. alexis* and *O. aygulus* it is tapered with a tip curvature considerably less than the radius of the lens cylinder at the base of the tip (figures 2 and 5). Screening pigment lines the distal margins of the facet cylinder in *O. westermanni* and to a lesser extent in *O. alexis*, but is absent in *O. aygulus*.

Table 1. Dimensions of corneal facets in ventral eye (in micrometres)

(Measurements were made on about equal numbers of sections of fresh and plastic-embedded corneas. No difference could be detected between these two sets of data, so they were pooled. Only the facets in the central region of the cornea were measured, since in some species the cornea is thicker at the eye margins. Each value is the mean and s.d. of at least 10 measurements made on sections of corneas of four to six specimens of each species.)

species	*O. westermanni*	*O. alexis*	*O. aygulus*
thickness	60±2	45±2	51±2
distal diameter†	39±1	37±1	37±1
proximal diameter	37±1	33±1	34±1
distal curvature	49±2	48±2	77±5
proximal curvature	−12→−16	−19→−13	−8→−13
length of proximal tip	12±1	13±1	16±1
length of distal homogeneous region	22±2	10±1	13±2
length of lens cylinder‡	38±1	35±1	37±3
extent of corneal screening pigment	distal third of facet	distal fifth of facet	none to very faint

† Diameter at the junction between the lens cylinder and the proximal corneal tip (g.h. region in figure 13).
‡ Includes length of proximal corneal tip.

A crystalline cone lies directly beneath each corneal facet. It is a solid structure that has the overall appearance of a bullet (figures 2, 5 and 7). Because of the importance of the crystalline cone in superposition-image formation and in our modelling of the compound eye, the dimensions of cones from the three species were carefully measured (table 2). Although the cones of the three species are similar in size, some notable differences exist. Firstly, the degree of insertion of the distal end of the crystalline cone into the proximal corneal tip differs in the three species. In *O. aygulus* and *O. alexis* the distal end of the crystalline cone is concave and deeply inserted into the curved corneal tip (figures 2 and 5); in *O. westermanni* it is fairly flat with only a slight central depression where it abuts the corneal tip (figure 7). Secondly, the cone waist, the junction between the distal tapered region and the proximal elliptical tip of the crystalline cone, differs in the three species. In *O. aygulus* it is absent, in *O. alexis* it is very slight, whereas in *O. westermanni* a strong waist is present (figures 2, 5, 7 and 11, table 2).

The walls of the crystalline cones and the spaces between the proximal tips of the corneal lenses are lined with screening-pigment granules. These granules, particularly numerous in *O. westermanni* (figure 7), occur predominantly in the proximal region of the crystalline-cone layer, but do not cover the proximal tips of the cones.

TABLE 2. DIMENSIONS OF CRYSTALLINE CONES IN VENTRAL EYE (IN MICROMETRES)

(All measurements made on fresh cones in saline. *N* is the number of beetles examined.)

	O. westermanni ($N = 5$–9)	*O. alexis* ($N = 5$)	*O. aygulus* teneral ($N = 5$)†	*O. aygulus* mature ($N = 3$)
length	77.8±4.8	76.2±1.0	83.3±1.5	82.7±1.1
maximum distal diameter	28.6±0.8	26.4±0.6	27.1±0.8	26.9±0.5
waist diameter	20.2±0.7	20.3±0.5	21.5±0.6	21.7±0.5
distance of waist from proximal tip	38.8±1.4	32.8±1.5	35.8±2.0	39.3±2.3
diameter of proximal tip ($2y_e$)	22.3±0.7	21.7±0.3	21.5±0.5	22.4±0.8
distance of maximum tip diameter from proximal tip (x_e)	20.8±1.9	18.0±1.8	20.6±1.9	23.1±1.0
tip ellipticity (y_e/x_e)	0.54±0.04	0.61±0.06	0.52±0.03	0.48±0.02

† Less than 60 h after adult ecdysis. The immature cones of *O. aygulus* differ from the mature cones only in the dimensions of the proximal tip. During the first few days of adult life, the proximal tip grows slightly in size and the waist moves to a more distal position.

The crystalline cones are separated from the rhabdom layer by a wide clear zone consisting of the columns of the retinular-cell extensions, each column surrounded by six secondary-pigment cells (although devoid of pigment granules in the clear zone). The retinular-cell nuclei lie distally, immediately beneath the proximal tips of the crystalline cones. The width of the clear zone differs in the three species (figures 1, 4 and 6). It is widest in *O. aygulus* and thinnest in *O. westermanni* (table 3).

The diameters of the retinular-cell extensions increase at the proximal margin of the clear zone to form the rhabdoms. Each rhabdom is a fluted cylinder topped with a single distal rhabdomere. In transverse section each rhabdom is seen to be strongly lobed, and the six evenly spaced lobes give it an asterisk-like appearance (figure 8). The rhabdom appears to be constructed according to the standard 1+6+(1) rhabdomere formula also found in chafer

DESCRIPTION OF PLATE 1

FIGURES 1–3. Structure of the ventral compound eye in *Onitis aygulus*.

FIGURE 1. Radial section through the eye in the dorso-ventral plane, showing the spatial arrangement of the cornea (co.), crystalline cones (c.c.), the underlying clear zone (c.z.) and the rhabdom layer (r.l.). Retinular-cell extensions (r.e.) can be seen spanning the clear zone, which is particularly wide in this species. The eye is enclosed in a capsule formed dorsally by the canthus (ca.) and elsewhere by a simple cuticular invagination. The rhabdom layer rests proximally on a basal lamina (b.l.). Scale bar 100 μm.

FIGURE 2. Longitudinal section along the axis of two corneal facets and crystalline cones showing the tight insertion of the distal cone into the inner corneal surface. Screening pigment (s.p.) optically isolates the crystalline cones. Scale bar 20 μm.

FIGURE 3. Rhabdoms cut longitudinally to show the presence of a distal rhabdomere (rh.), and screening pigment (s.p.) lining the proximal one-fifth of the rhabdoms. The perforated basal lamina (b.l.) is evident. Scale bar 20 μm.

PHILOSOPHICAL TRANSACTIONS OF THE ROYAL SOCIETY B BIOLOGICAL SCIENCES

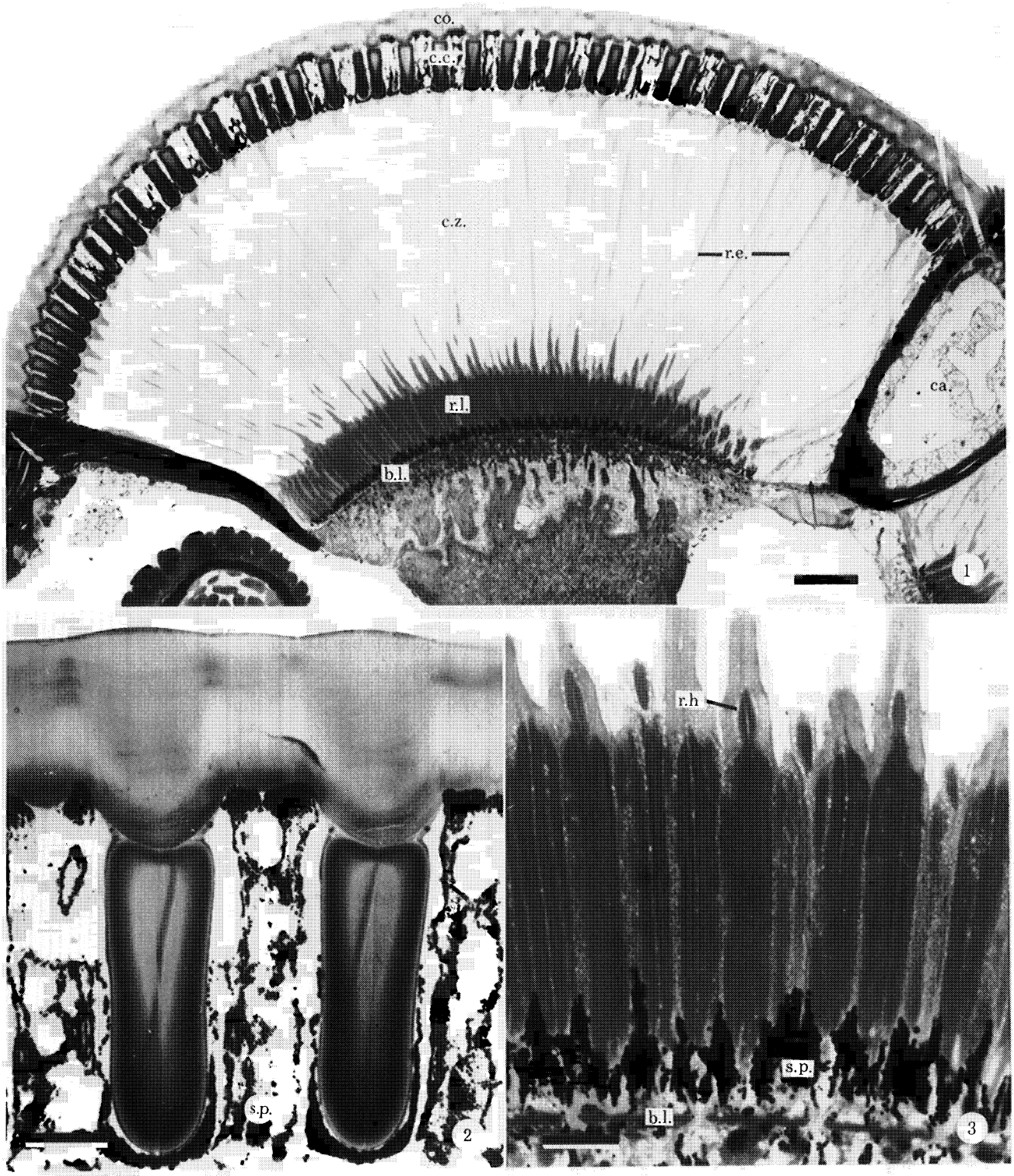

FIGURES 1–3. For description see opposite.

(*Facing p.* 242)

PHILOSOPHICAL TRANSACTIONS OF THE ROYAL SOCIETY B BIOLOGICAL SCIENCES

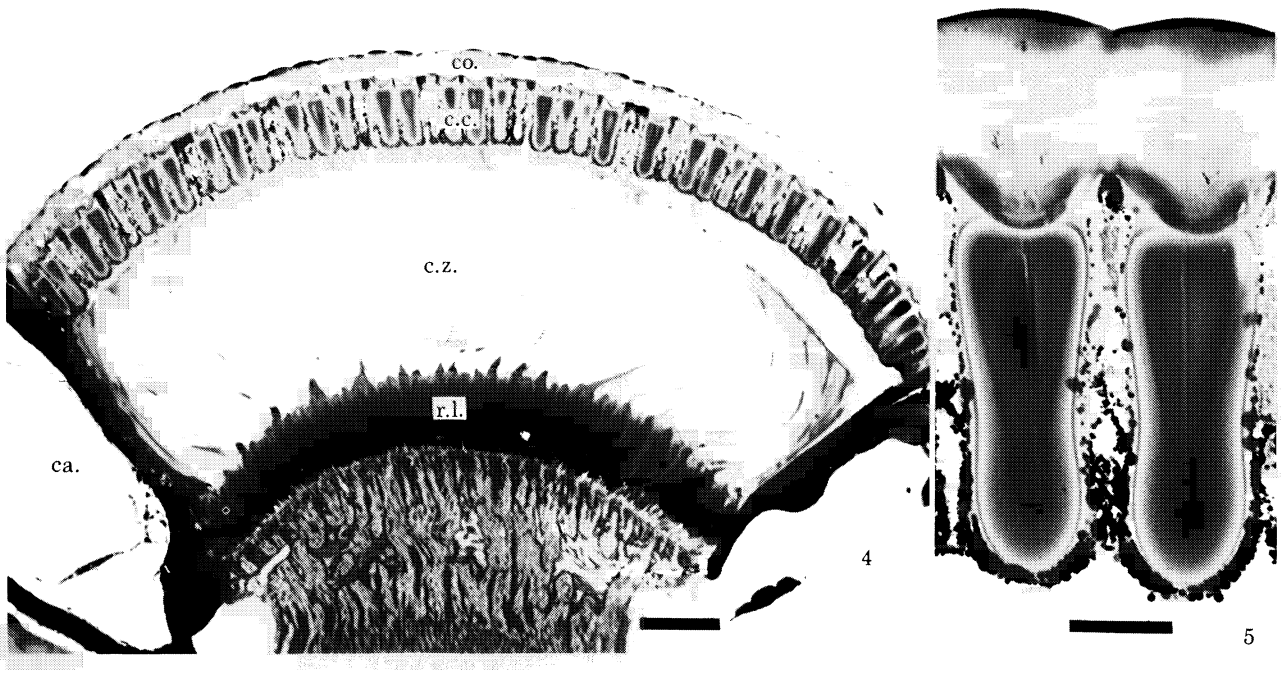

FIGURES 4 AND 5. Ventral compound eye of *O. alexis*. Abbreviations as in figures 1–3.

FIGURE 4. Section as in figure 1, at the same magnification, to show the relationship between the elements of the eye. The facets have a greater curvature in this species and the clear zone is proportionally thinner. The clear zone has partly separated from the cone layer during fixation. Scale bar 100 μm.

FIGURE 5. Corneal facets and crystalline cones cut longitudinally. The stronger facet curvature is clear in this micrograph, as is the looser insertion of the crystalline cones into the inner surface of the corneal facets. Scale bar 20 μm.

DESCRIPTION OF PLATE 3

FIGURES 6–8. Compound eye of *O. westermanni*. Abbreviations as in figures 1–3.

FIGURE 6. Radial section through the ventral eye (left) and oblique section through the dorsal eye (right), the eyes separated by the canthus. This species had the narrowest clear zone of the three species studied. Scale bar 100 μm.

FIGURE 7. Longitudinal section through the corneal facets and crystalline cones. In this species the inner surface of the corneal facets are less strongly curved and the crystalline cones are only slightly inserted into the cornea. The cones are screened strongly by pigment granules except where the cone cells and retinular cells (r.c.) attach. The centres of curvature of the corneal facets (+) do not lie on the axes of the corneal lenses, but are displaced towards the canthus edge of the eye (towards the right). Scale bar 20 μm.

FIGURE 8. Rhabdoms in slightly oblique transverse section. The asterisk-shaped rhabdoms are hexagonally packed and the lobes of the individual rhabdoms almost touch. Near the clear zone (c.z.) only the distal rhabdomere (rh.) is seen in the section; more proximally this rhabdomere appears to form one of the lobes of the rhabdom. The basal lamina appears in this section (though not shown in the micrograph) at the lower left. Scale bar 20 μm.

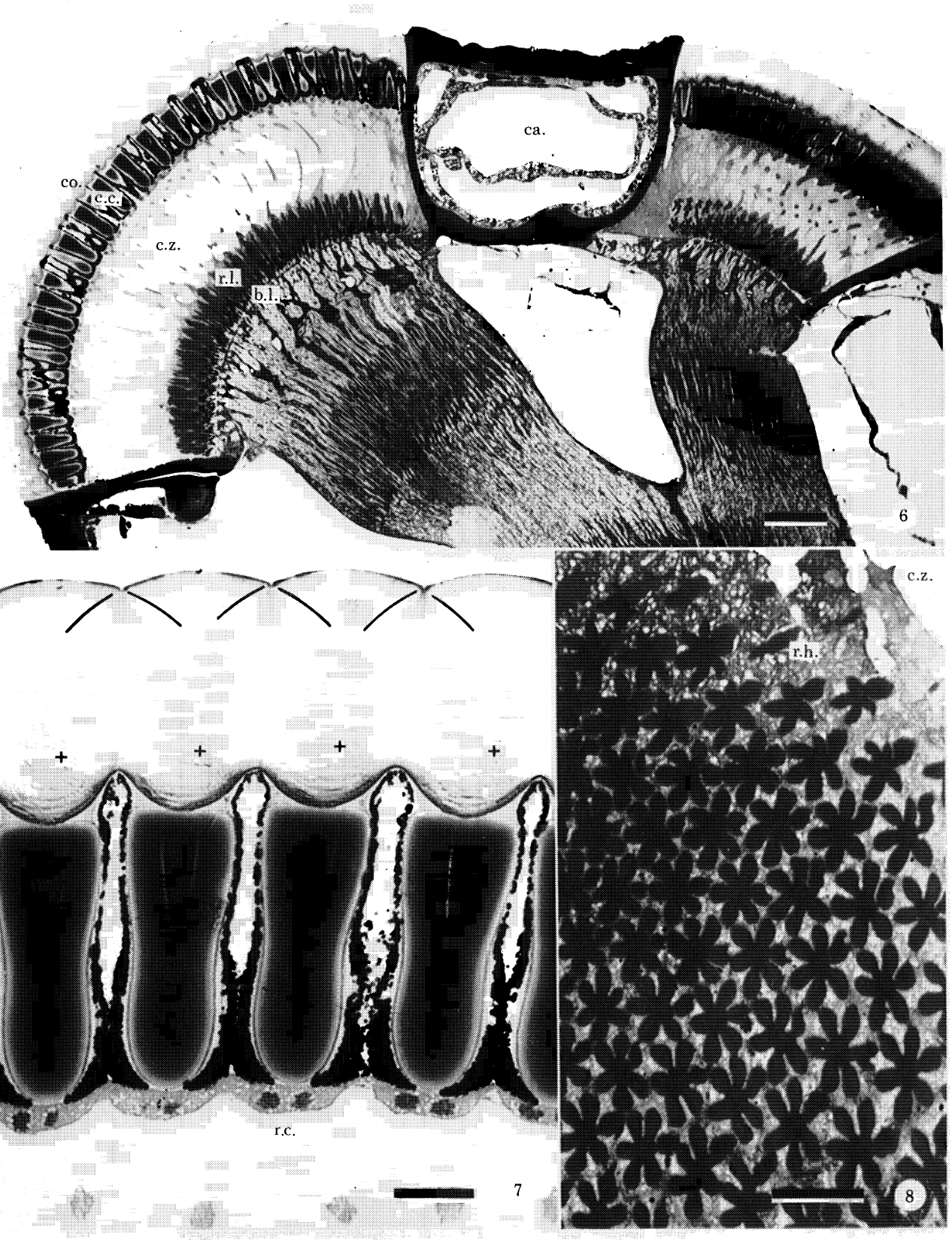

FIGURES 6–8. For description see opposite.

PHILOSOPHICAL TRANSACTIONS OF THE ROYAL SOCIETY B BIOLOGICAL SCIENCES

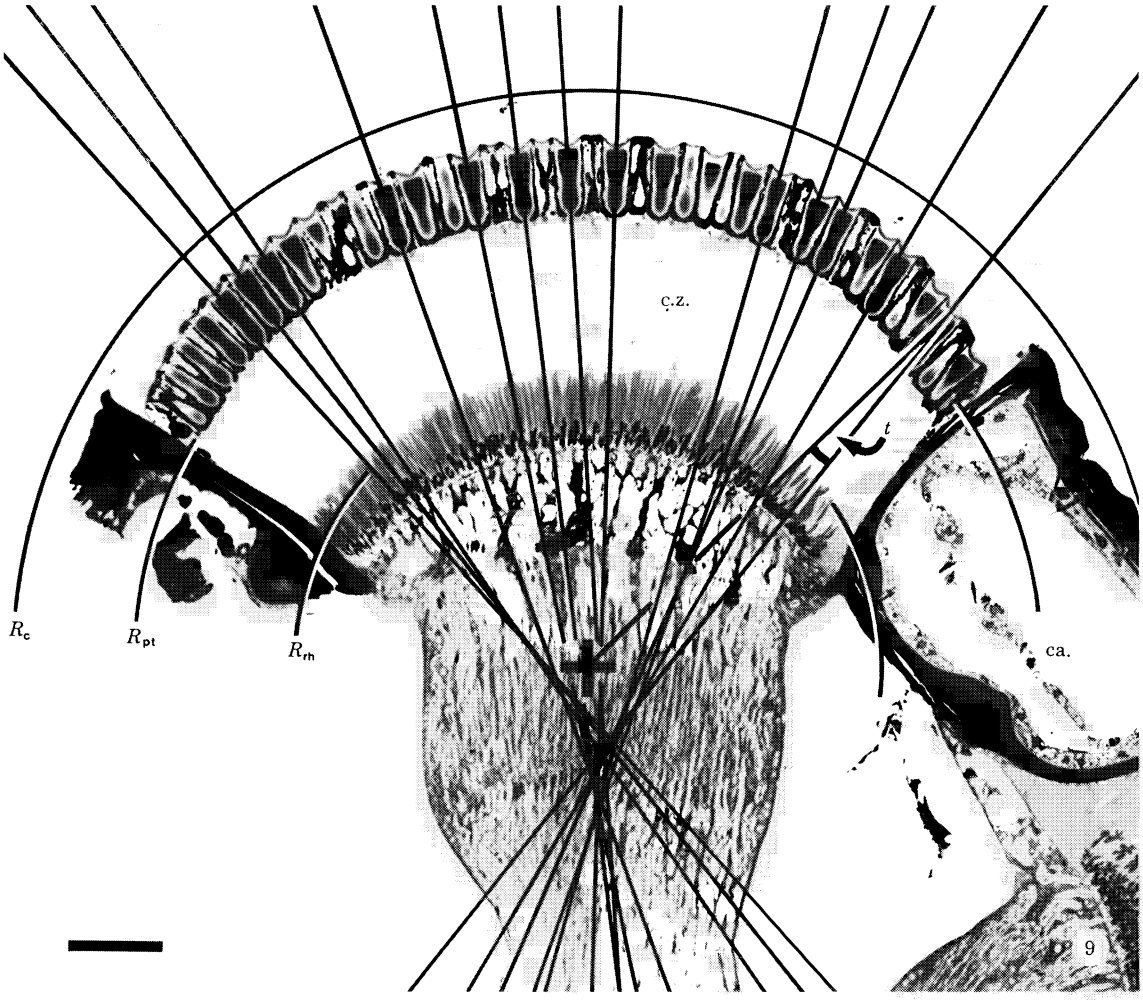

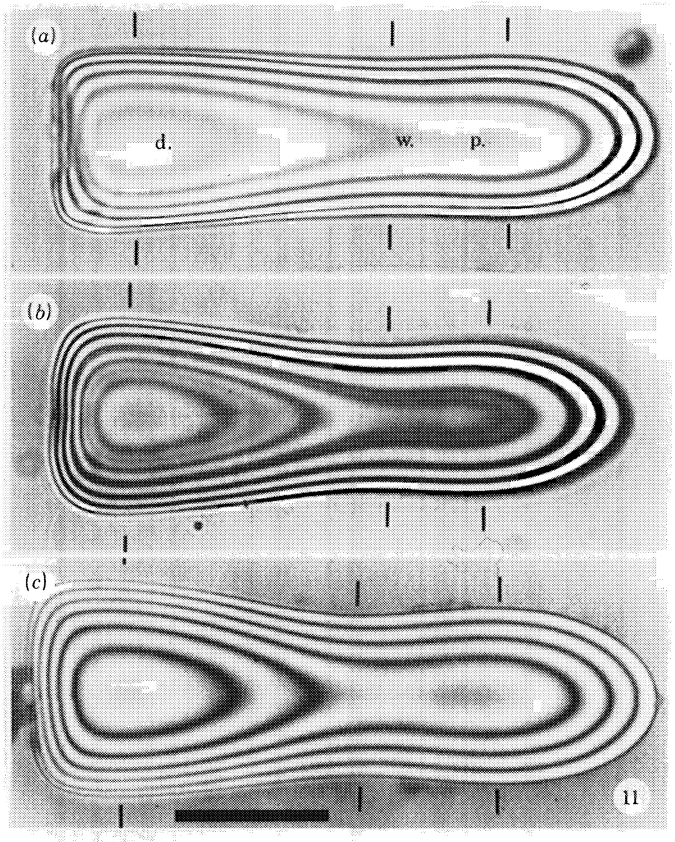

FIGURES 9 AND 11. For description see opposite.

PHILOSOPHICAL TRANSACTIONS OF THE ROYAL SOCIETY B BIOLOGICAL SCIENCES

beetles (Meyer-Rochow 1977; Gokan 1982) in which one rhabdomere lies slightly more distal to the six that constitute the bulk of the rhabdom cylinder. The distal rhabdom is clearly visible in *O. aygulus* (figure 3). A basal rhabdomere was not detected at the light microscopical level. The basal quarter of the rhabdom is surrounded by granules of screening pigment in all three species (figures 1, 3, 4 and 6). No tracheal tapetum, and consequently no eyeshine, is present in this genus of dung beetle, although common in other scarab eyes (Gokan 1973).

(*b*) *Optical geometry of the beetle eye*

In a superposition eye with spherical symmetry, the various layers of the eye, the cornea, crystalline-cone layer and rhabdom layer, have a common centre of curvature, with the long axes of the crystalline cones intersecting this point. The geometrical relationship between the lens elements and the rhabdom layer determines the optimal angular magnification (M) for superposition-image formation (Caveney & McIntyre 1981).

Perfect spherical symmetry is not present in the ventral eyes of *Onitis*, as the rhabdom layer is not concentric with the lens layer. The width of the clear zone, relative to the curvature of the lens layer, is a better indicator of M. The optical geometry of the eyes in the three *Onitis* spp. is summarized in table 3, which includes values for the eyes featured in figures 1, 4 and 6. *O. aygulus* has the widest, and *O. westermanni* the narrowest, clear zone. As a consequence, *O. aygulus* requires the lowest M (0.95, 0.97) to form a superposition image at the rhabdom level, and *O. westermanni* the highest M (1.83, 1.96). The eye of *O. alexis* is intermediate between these two species in both its size and optical geometry.

At the edges of the eye the local radius of curvature of the cornea is less than that over the rest of the eye. This is particularly pronounced in *O. westermanni* (figure 9, plate 4). Consequently the curvatures listed in table 3 are from the central three quarters of the eye.

In addition, the centre of curvature of the outer surface of the individual corneal facets does not always lie along the long axis of the corneal lens, but is frequently displaced towards the canthus margin of the eye. This too was particularly noticeable in *O. westermanni* (figure 7).

Description of plate 4

Figure 9. Deviation from spherical symmetry in the eye of *O. westermanni*. The centre of curvature of the eye (+) was determined from the radius of curvature of the layer formed by the proximal tips of the crystalline cones (R_{pt}). Only close to the canthus (ca.) is this layer not centred on this point. The outer surface of the cornea (radius of curvature R_c) is concentric with the cone-tip layer, except at the edges of the eye, where the curvature is tighter. The long axes of the crystalline cones, however, project inwards towards a region proximal to the centre of curvature of the eye. The angle of cone tilt (t) is maximal at the margin of the eye. The rhabdom layer has a curvature shallower than that predicted in a spherically symmetrical eye (R_{rh}). As a consequence, the clear zone (c.z.) is widest in the central region of the eye. Scale bar 100 μm.

Figure 11. Interference micrographs of intact crystalline cones of (*a*) *O. aygulus*, (*b*) *O. alexis* and (*c*) *O. westermanni*. The cones were freshly removed, immersed in saline ($n = 1.336$) and photographed in green ($\lambda = 550$ nm) (*a*, *c*) or white light (*b*). The three sets of vertical bars indicate the axial levels at which the refractive-index profiles of the intact cones were measured (see figure 12). d., Distal region; w., waist; p., proximal tip.

Although the cones of the three species have a similar number of interference fringes at each of the levels measured, the spacing between the fringes is not the same. Fringe spacing decreases rapidly towards the edge of the cone in (*a*) but less so in (*c*). Differences in fringe spacing are caused by differences in the refractive-index profile in the cones of the three beetles.

The distal (left) ends of the crystalline cone insert into the corneal tip. In (*a*), the crystalline cone is deeply inserted, in (*c*) it is only slightly inserted into the cornea. Scale bar 20 μm.

PHILOSOPHICAL TRANSACTIONS OF THE ROYAL SOCIETY B BIOLOGICAL SCIENCES

Table 3. Optical geometry data

(M_0 is the angular magnification required to give a focus at the distal tips of the rhabdoms in the central region of the eye: $M_0 = (R_{pt}/\text{clear-zone width}) - 1$. $\Delta\rho_R$ is the angular width of the rhabdoms, equal to the diameter divided by the posterior nodal distance f, which is the radius of curvature at the distal rhabdom tips (Land *et al.* 1979). The interommatidial angle $\Delta\phi$ was measured from eye sections as in figures 1, 4 and 6. The rhabdom data were also taken from sections (as in figures 3 and 8). Most of the data listed are from individual beetles, as body size and hence eye size, are quite variable in these species. Dimensions in micrometres and angles in degrees.)

species	*O. westermanni* (1)	*O. westermanni* (2)	*O. alexis* (1)	*O. alexis* (2)	*O. aygulus* (1)	*O. aygulus* (2)
radius of curvature of corneal surface (R_c)	608	688	756	728	978	1010
radius of curvature at level of proximal tips of cones (R_{pt})	480	560	640	620	864	887
clear-zone width in centre of eye	162	198	280	276	444	450
M_0	1.96	1.83	1.29	1.25	0.95	0.97
radius of curvature of distal rhabdom layer (f)	318	362	360	344	420	437
rhabdom diameter (d)	15–16		14		13	
$\Delta\rho_R$ (d/f)	2.7–2.9	2.4–2.5	2.2	2.3	1.8	1.7
interommatidial angle $\Delta\phi$	3		2.5		2.0	
rhabdom centre-to-centre spacing	15		14		13	
rhabdom length	65		86		94	

The alignment of the crystalline cones also deviates from spherical symmetry. This is most noticeable towards the margins of the eye, where the axes of the crystalline cones are clearly seen to be centred on a point proximal to the centre of curvature of the eye layers (figure 9). The maximum angle of the cone tilt is about 10°. This feature was seen in all three species. It is unlikely that the alignment of the cones is an artefact caused by tissue fixation and processing. In *O. westermanni*, many of the crystalline cones obtained from freshly dissected eyes have a distal surface not normal to the cone axis (figure 11*c*), suggesting that they are tilted in the living eye. In *O. aygulus*, this tilted alignment appears in the eye during its formation in the pupa (S. Caveney, personal observation). Even when the eye is accidentally distorted during fixation, the local geometry of the crystalline cones and overlying cornea is maintained.

Finally, the rhabdom layer is flatter and consequently the width of the clear zone less at the ventral margin of the eye than elsewhere (for example, figures 1 and 9).

(*c*) *Refractive-index gradients*

(i) *Cornea*

In most dung beetles, the body of the corneal facet is divided into an outer region, homogeneous in refractive index and an inner g.r.i. region (Caveney & McIntyre 1981). The position and extent of these two regions may be determined from longitudinal sections of facets viewed in the interference microscope. In *O. aygulus* and *O. alexis* the homogeneous region is relatively thin, and in *O. westermanni* relatively thick, compared with the total corneal thickness (table 1).

To measure refractive-index distribution in the cornea, tangential sections were cut through the facets. Quantitative measurements were made on sections of cornea from *O. alexis* and *O. westermanni* only. In *O. alexis* the homogeneous region of the facet (figure 10*a*) and the bulk

of the distal section of the g.r.i. lens cylinder (figure 10*b*) have a refractive index of about 1.527. The edge refractive index in the latter region is about 1.501. The g.r.i. lens is most strongly developed at the proximal end of the corneal facet. While the axial refractive index remains high in this region (1.526), that of the facet edge drops to about 1.475 (figure 10*c*). The profile of the refractive-index gradient here is almost parabolic. Similar values were obtained for the lens-cylinder region in *O. westermanni*. In general, the features of the corneal g.r.i. lens in *Onitis* are similar to those reported for another scarab beetle, *Anoplognathus* (Caveney & McIntyre 1981).

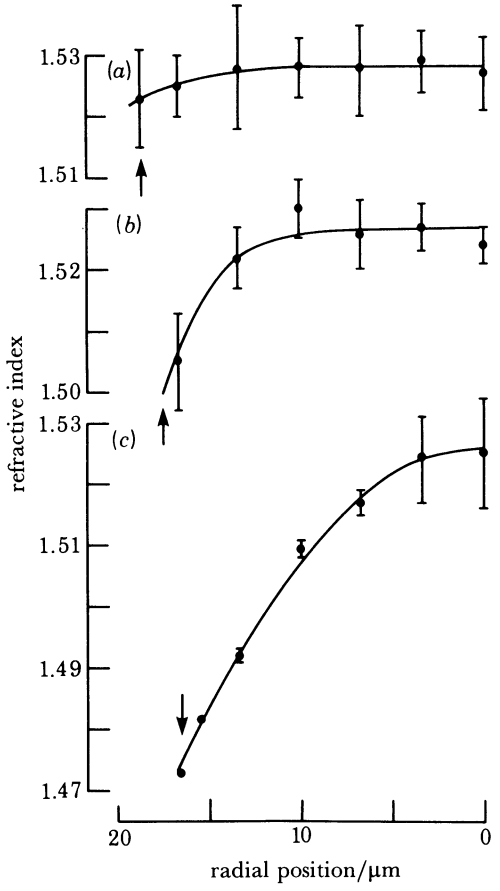

FIGURE 10. Refractive-index scans across the main regions of the corneal facet of *O. alexis*. The profiles were determined interferometrically from transverse sections of (*a*) the distal cornea ($N = 4$); (*b*) the distal region of the lens cylinder ($N = 5$); and (*c*) the proximal lens cylinder and corneal tip ($N = 2$). The vertical arrows mark the approximate position of the boundary in the three regions. Curves were fitted to the data assuming a refractive-index profile of the form $n(r) = n_0(1 - ar^{\alpha})$. The fit values are:

region	α	n_0	n_b	R^2
(*a*)	8	1.528	1.523	0.899
(*b*)	8	1.527	1.501	0.944
(*c*)	2	1.526	1.475	0.996.

Only in the proximal region of the cornea is the refractive-index gradient parabolic ($\alpha = 2$). R^2 is the coefficient of determination.

The refractive-index profiles of corneal slices are hard to measure accurately, owing to variations in section thickness and difficulties involved with the double-immersion technique used. Nevertheless the values obtained were adequate to model the cornea, as they were used

in conjunction with measurements of the back focal distance and back focal length of intact corneal facets.

(ii) *Crystalline cones*

All refractive-index determinations were done on intact crystalline cones similar to those shown in figure 11; the data are summarized in figure 12. The distal region of the cone in all three species has the highest axial refractive index, with means ranging between 1.489 and 1.494. Similarly, the axial refractive index in the proximal cone tip in the three species has a narrow range, with means between 1.464 and 1.469. In the waist region the axial refractive index showed greater variation, with the lowest value in *O. westermanni* (1.470) and the highest in *O. aygulus* (1.488). The refractive index at the boundary of the crystalline cones, irrespective of level scanned, varied between 1.340 and 1.350. These values suggest that the cone-axis and boundary refractive indexes are set at similar values in the three species during development (with the notable exception of the axial refractive index in the waist region).

The manner in which the refractive index drops off towards the cone boundary in the waist and proximal regions differs in the three species. In *O. westermanni*, the refractive-index gradient is parabolic ($\alpha = 2$) in these two regions (figure 12). In *O. alexis* it is flatter than parabolic near the axis but steeper than parabolic near the boundary of the crystalline cone (figure 12: $\alpha = 2.5$ in the waist region, $\alpha = 2.5$–2.75 in the proximal region). This trend is also seen in *O. aygulus* (figure 12: $\alpha = 2.6$ in the waist region, $\alpha = 2.75$ in the proximal region). It was noticed during the course of the measurements on *O. aygulus* that the gradient shapes in these two regions of the crystalline cone change considerably in the first week after adult ecdysis. During the first few days of adult life, the cones, although almost normal in shape (table 2), have low axial refractive indices and high α values. Only when the adult is about a week old do the refractive-index gradients begin to stabilize. The data presented in figure 12 are from mature cones. The main difference between the mature cones of *O. aygulus* and *O. alexis* is the degree to which the axial refractive index drops between the distal and waist regions. The refractive-index profiles in the *O. westermanni* cone are clearly distinct from those of the other two species. This can be inferred *a priori* from the differences in the interference fringe spacings in the cones shown in figure 11.

(*d*) *Ray-tracing model*

Ray tracing was carried out on a computer. The corneal lens and crystalline cone were each divided into three regions as shown in figure 13. The dimensions of these regions differ from species to species: values for the three species examined here are given in tables 1 and 2. Outside the eye is air ($n = 1.00$) and inside the clear zone ($n = 1.34$). A ray is refracted at the curved outer surface of the cornea, passes through a homogeneous region whose refractive index is n_0 and into the g.r.i. lens-cylinder region. There the refractive index drops from a maximum value of n_0 on axis to its minimum value at the boundary, this gradient causing the ray to bend. The form of gradient used is

$$n(r) = n_0(1 - ar^{\alpha}), \tag{1}$$

where the parameters a, α are chosen to fit the measured corneal data (figure 10). The gradient in the third region of the cornea, the g.r.i. hemisphere, is also given by (1), but with r now the distance from the centre of curvature of the back corneal surface. The same α is used for both regions. The ray is refracted at the back corneal surface and again at the distal surface

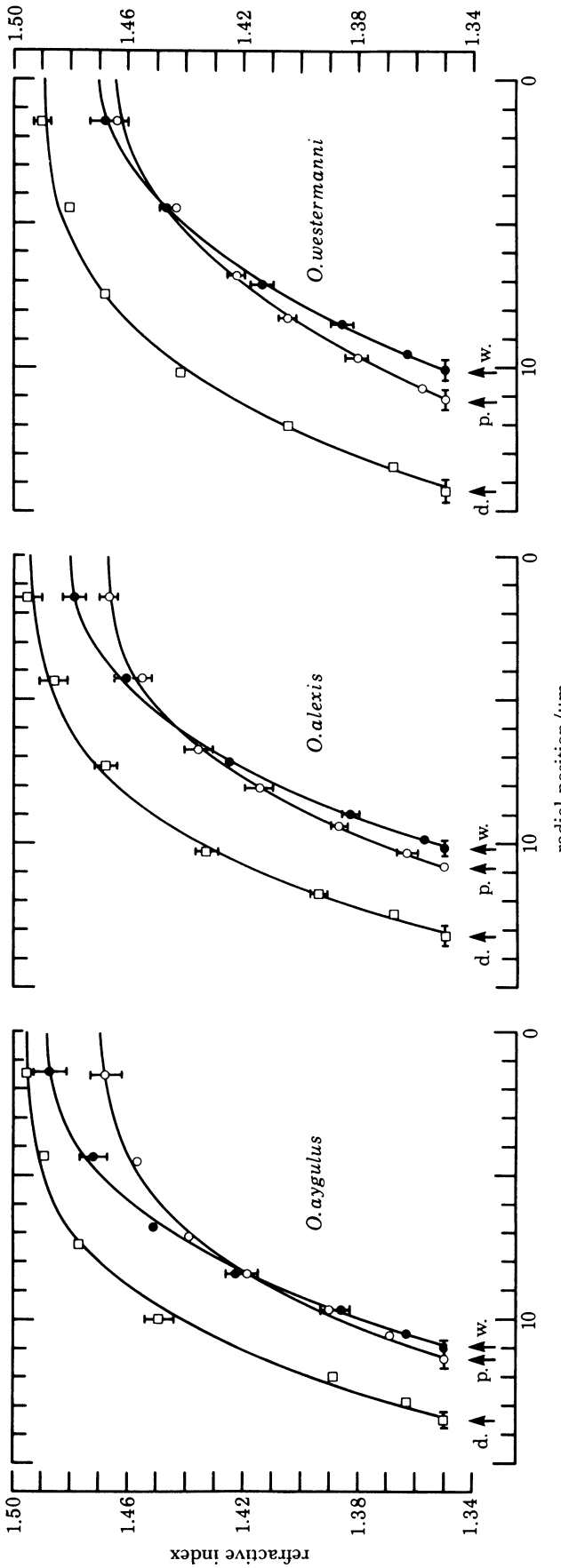

FIGURE 12. Mean curves of the distribution of refractive index across the crystalline cones of *O. aygulus*, *O. alexis* and *O. westermanni*. The refractive-index distribution is shown for the distal region (squares), waist (filled circles) and proximal tip (open circles) of the crystalline cones, as indicated in figure 11. The horizontal axis is the radial position in the cone, the cone radius in each region being the mean value in table 2 (marked here as vertical arrows). Symbols show the mean refractive index (±s.d.) versus radial position in each cone region. The horizontal error bars are the s.d. of the cone radii (not drawn where they are smaller than the symbols). The data were fitted assuming a refractive-index profile of the form $n(r) = n_0(1-ar^\alpha)$ (solid lines). R^2 is the coefficient of determination. Fit parameters are shown below.

	region	α	n_0	R^2
O. aygulus ($N = 2$)	distal	3.5	1.494	0.994
	waist	2.6	1.488	0.997
	proximal	2.75	1.469	0.997
O. alexis ($N = 5$)	distal	3.0	1.494	0.994
	waist	2.5	1.480	0.999
	proximal	2.75	1.467	0.998
O. westermanni ($N = 6$)	distal	3.0	1.489	0.997
	waist	2.0	1.470	0.998
	proximal	1.9	1.464	0.998

of the crystalline cone. This consists of a depression concentric with the back surface of the cornea and a flat annular region (figure 13). Ray tracing in the cone then proceeds as in the cornea; first a homogeneous region (of refractive index n_{0c}), followed by a g.r.i. lens-cylinder region with a gradient of the form (1) (but with n_0 replaced by n_{0c} and different a, α values), and finally a g.r.i. hemi-ellipsoidal region. There the gradient is given by

$$n(r, z) = n_0(1 - a[(r/r_B)^2 + (z/z_B)^2]^{\alpha/2}), \quad (2)$$

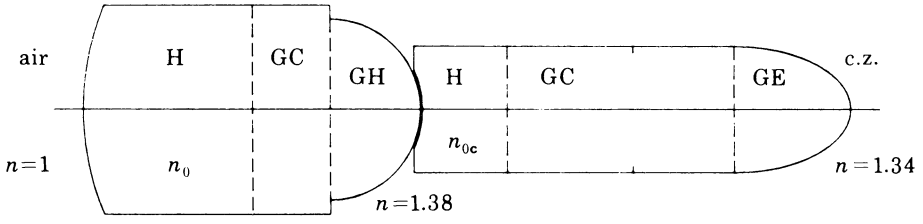

FIGURE 13. Model ommatidium used in ray tracing. The corneal lens and crystalline cone were each divided into three regions as shown by the vertical dashed lines: a homogeneous region (H), a g.r.i. lens-cylinder region (GC) and a g.r.i. hemisphere (GH) in the cornea or g.r.i. ellipse (GE) in the cone. c.z., Clear zone. The two short vertical lines indicate the waist of the crystalline cone.

where z is the co-ordinate along the axis; r perpendicular to the axis, with the origin at the start of the ellipsoidal region (right-hand dashed vertical line in the cone in figure 13); r_B, z_B are the maximum values (reached at the cone boundary) of r, z, and the power α is the same as used in the lens-cylinder region of the cone. Surfaces of equal refractive index are therefore concentric with the back surface of the cone and are continuous across the boundary between the lens-cylinder region and the ellipsoidal region. On reaching the back surface of the cone, the rays are refracted (but only very slightly because of the small drop in refractive index) into the clear zone.

In the regions with refractive-index gradients (GC, GH, GE in figure 13), rays were traced by solving the ray equation numerically by using the method of Meggitt & Meyer-Rochow (1975). In two dimensions all rays are meridional rays (ray plots in figures 14–16).

In the first step of the modelling, rays were traced through the cornea alone, with the refractive index behind the cornea that of physiological saline (1.336). The corneal parameters of the model were set to those measured (table 1), with the values for the refractive-index gradient those measured at the proximal end ($n_0 = 1.53$, $n_b = 1.47$: figure 10). The length of the homogeneous region was then adjusted about the measured value (keeping total length constant) until the values for the back focal distance s' and back focal length f' calculated for the model were close to those measured (table 5). The length used is larger than that of the actual homogeneous region (table 1), because in the model there is a sharp division between the homogeneous region and the g.r.i. region with $\alpha = 2$, whereas in the actual lenses there is a transition. Values of α decrease from large values near the actual homogeneous region to a value of 2 more proximally (figure 10).

Having found acceptable corneal parameters, the crystalline cone was added. The gradient parameters for the g.r.i. regions (figure 13) were set at those measured in the waist–proximal region (see table 4, cf. caption to figure 12). The homogeneous region, with length initially set to the distance from the distal tip of the crystalline cone to the level marked d in figure 11, models the complicated gradient indicated in figure 11. The overall gradient in the cone, with

Table 4. Parameters used in the computer models

(L is a length; H is homogeneous region; G is g.r.i. region (see figure 13); D is diameter; R_1, R_2 are the radii of curvature of the outer and inner surfaces respectively of the corneal lens; S_{ep}, distance between cornea and cone; W_C, width of the curved part of the distal end of the cone; x_e, length of the elliptical tip of the cone (GE in figure 13). All lengths in micrometres.)

parameters	*O. westermanni*	*O. alexis*	*O. aygulus*
cornea			
n_0	1.530	1.530	1.530
n_b	1.470	1.470	1.470
L_H	30.0	25.0	20.0
L_G	29.8	20.4	30.5
D	37.0	35.0	36.0
R_1	48.0	45.0	77.0
R_2	−16.0	−11.0	−9.0
α	2.0	2.0	2.0
S_{EP}	0.4	0.5	0.5
cone			
n_{0c}	1.470	1.470	1.469
n_{bc}	1.350	1.350	1.350
L_H	15.0	10.0	1.0
L_G	62.8	66.6	76.5
D	22.4	21.8	22.4
W_C	7.0	7.0	8.0
x_e	20.8	18.0	23.1
α	2.0	2.5	2.6
eye			
f	320	350	430
R_{pt}	480	630	870

α values decreasing from distal to proximal, was thus modelled as a homogeneous region together with a g.r.i. region with fixed α and fixed maximum and minimum refractive indexes. The length of the homogeneous region was adjusted slightly about the original value to fine tune the model. At this stage, the curvature of the back surface of the corneal lens was also adjusted slightly in *O. alexis* and *O. aygulus*. The final values for s', f' (that is, from the models used in figures 14–16) are those given in table 5. Table 4 gives the other parameters used in the models.

Rays were also traced in three dimensions by using the same method. The corneal lens, crystalline cone and their refractive-index gradients were assumed rotationally symmetrical about the optic axis. Parallel rays, incident on the cornea in a square grid with spacing 1.5 μm, were traced through the ommatidium, and the positions and angles at which each ray emerged from the proximal cone tip were stored by the computer. The spread of the total beam emerging from the cone tip could then be shown, as a spot diagram, at any position in the clear zone. The three-dimensional ray tracing includes all rays, that is, both meridional and skew rays.

To simulate the superposition image of a point source (parallel incident rays) formed by an eye, rays were traced in three dimensions through each ommatidium in turn, starting at the central ommatidium and stepping out until no rays emerged from an ommatidium. This defines the diameter of the aperture of the eye: the area (its diameter measured in number of ommatidia or in micrometres at the eye surface or angle subtended at the centre of the eye) through which light from one direction in space can reach the retina. The position and direction of each emerging ray was transformed to a coordinate system centred on the proximal cone tip of the

PHILOSOPHICAL TRANSACTIONS OF THE ROYAL SOCIETY B BIOLOGICAL SCIENCES

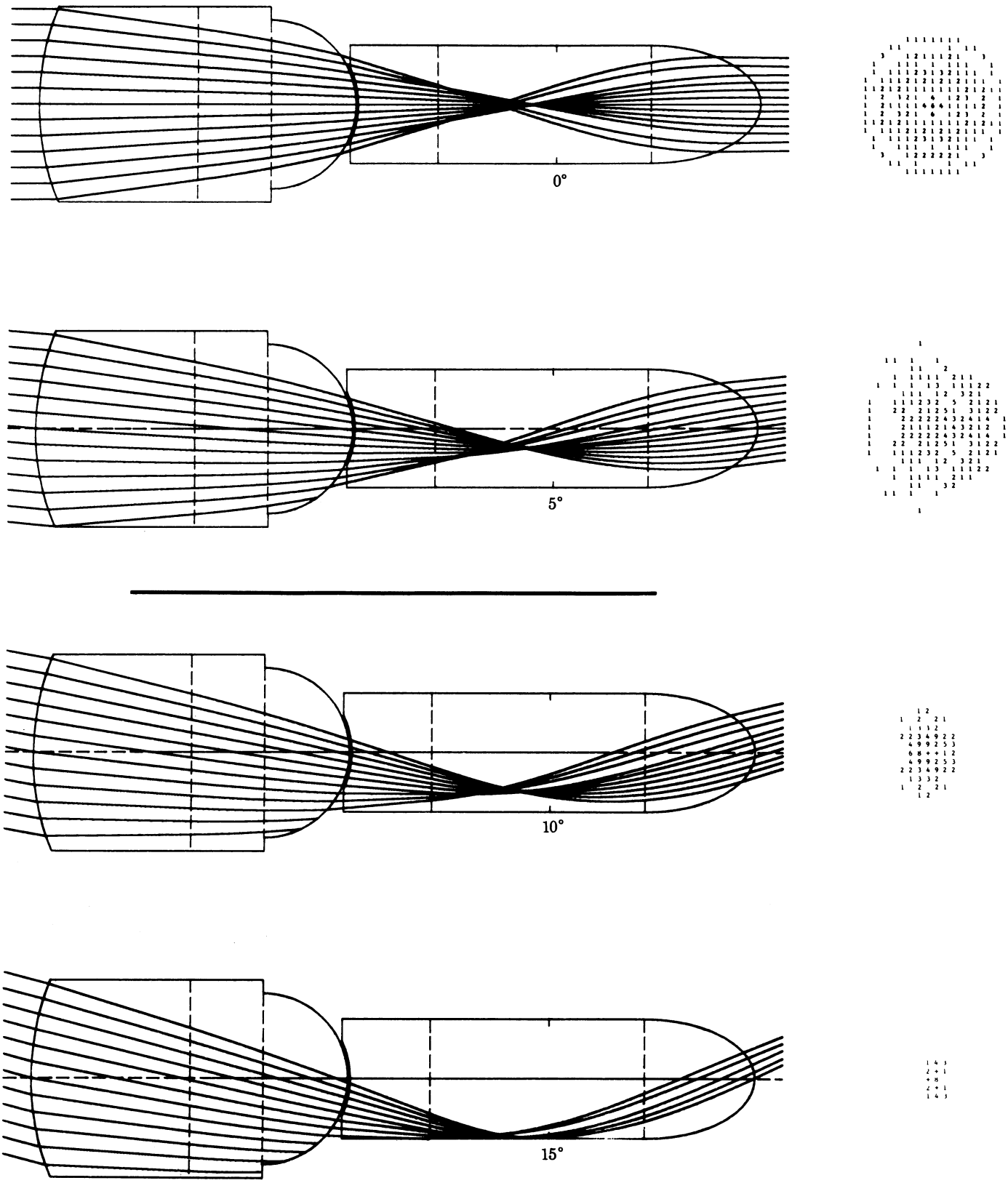

FIGURE 14. *O. westermanni*. For description see p. 253.

PHILOSOPHICAL TRANSACTIONS OF THE ROYAL SOCIETY B BIOLOGICAL SCIENCES

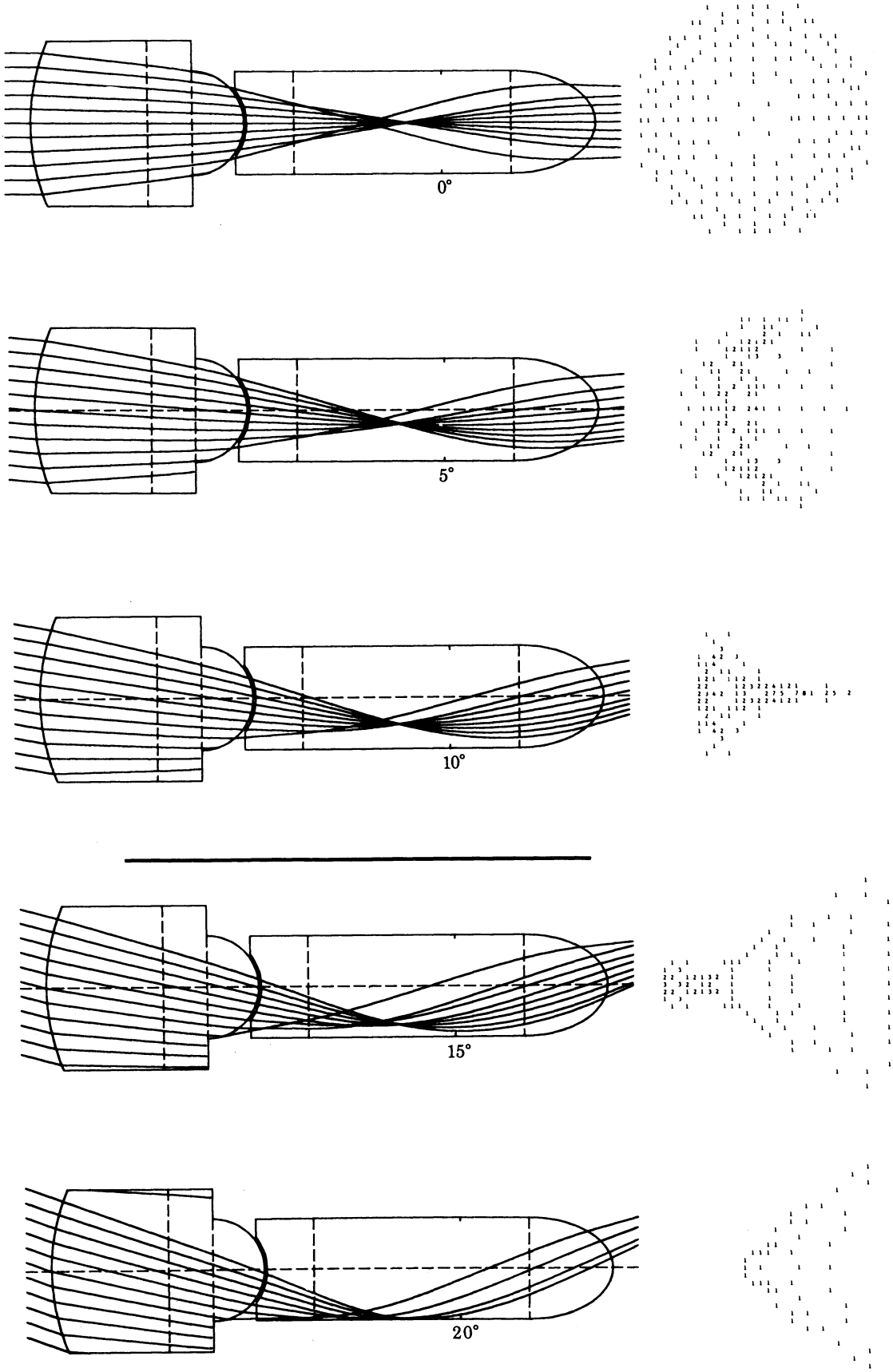

FIGURE 15. *O. alexis*. For description see p. 253.

PHILOSOPHICAL TRANSACTIONS OF THE ROYAL SOCIETY B BIOLOGICAL SCIENCES

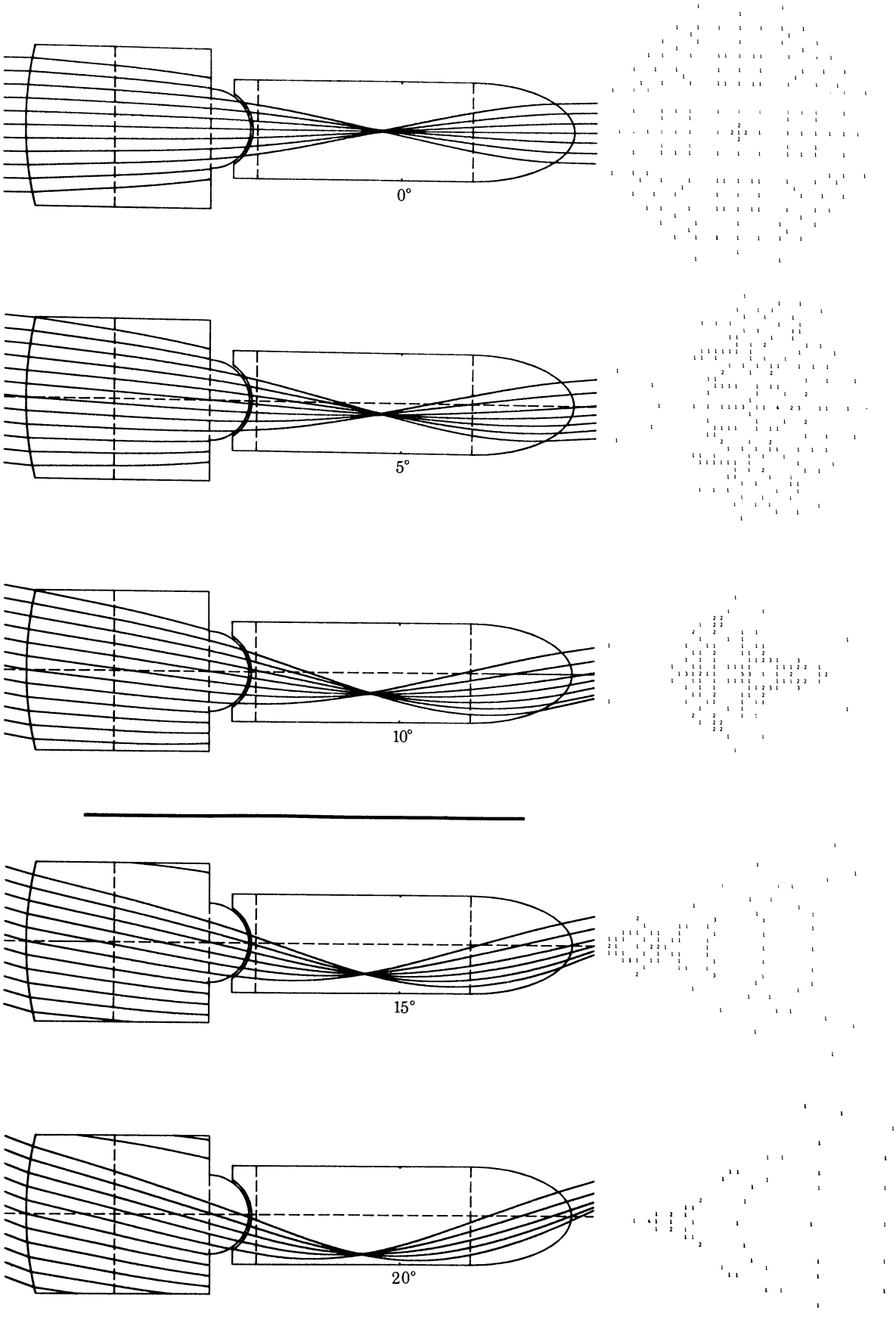

FIGURE 16. *O. aygulus*. For description see opposite.

PHILOSOPHICAL TRANSACTIONS OF THE ROYAL SOCIETY B BIOLOGICAL SCIENCES

TABLE 5. BACK FOCAL DISTANCES (s') AND BACK FOCAL LENGTHS (f') OF CORNEAL FACET LENSES MEASURED IN ISOLATED CORNEAS OF *ONITIS* AND CALCULATED FROM THE MODEL LENSES (FIGURES 14–16)

(The outer surface of the cornea was in air ($n = 1.000$) and the inner surface in saline ($n = 1.336$). N is the number of corneas examined; several facets were measured from each cornea.)

	s'		f'	
	measured	model	measured	model
O. westermanni ($N = 3$)	28 ± 2	28.5	52 ± 3	58.6
O. alexis ($N = 6$)	23 ± 2	26.8	44 ± 3	45.7
O. aygulus ($N = 6$)	22 ± 2	25.4	43 ± 2	39.1

central ommatidium. Spot diagrams could then be printed of the light distribution at different distances across the clear zone (figures 17–19). The position of best image was taken to be that at which the maximum number of rays passed through a circle lying directly below the central facet and of diameter that of the rhabdom. Spherical symmetry, with the ommatidial axes intersecting at the centre of curvature of the eye, was assumed in the model.

Paraxial focal lengths of the model lenses were obtained by tracing a ray incident at 0° and at a small distance r from the axis. If the ray is at angle θ to the axis when it eventually crosses it, the focal length is given by $r/\tan\theta$. Focal lengths of the second component of the ommatidial lens system, the proximal part of the crystalline cone, were obtained by tracing rays in the reverse direction to normal (Caveney & McIntyre 1981).

(*e*) *Ray-tracing*

(i) *Single ommatidia*

The results of ray tracing through the model ommatidial lenses are shown in figures 14–16 as two-dimensional ray traces with rays incident on the cornea at different angles, together with the corresponding light distribution (spot diagrams) at the level of the retina after a three-dimensional ray trace.

The corneal lens and distal part of the crystalline cone form the first component of a telescopic system (Caveney & McIntyre 1981), and together focus parallel incident rays to a position, the intermediate focus, just distal to the waist in the crystalline cone. In *O. westermanni* and *O. alexis*, the curved outer surface of the corneal lens provides a significant proportion (about 38%) of the refractive power of the first component, the g.r.i. regions being relatively thin. In *O. aygulus*, most of the refractive power (about 80%) comes from the refractive-index gradients in the cornea and distal cone; the homogeneous regions are significantly smaller than in the other two species.

DESCRIPTION OF FIGURES 14–16

FIGURES 14–16. Ray traces through the model ommatidia, with parameters based on the measured data. The left-hand column shows two-dimensional ray traces, with parallel rays incident at increasing angles (as indicated) to the ommatidial axis. Scale bar (horizontal) 100 μm. Small marks above the angles indicate the level of the waist in the crystalline cone.

The right-hand column shows the corresponding three-dimensional ray traces. A rectangular grid of rays is incident on the cornea. The rays are traced through the lenses and projected across the clear zone to the level of the best superposition image (see figures 17–19 and text). The spot diagrams show the number of rays in squares 1 μm × 1 μm and give the intensity distribution on the retina of the light that has passed through the ommatidium, as seen from the ommatidium. Scale bar (vertical) 20 μm. +, 10–19 rays; ♯ over 19 rays. Parameters used are given in table 4.

PHILOSOPHICAL TRANSACTIONS OF THE ROYAL SOCIETY B BIOLOGICAL SCIENCES

The back focal distance s' and back focal length f' of the isolated corneal lens decrease in the order *O. westermanni*, *O. alexis*, *O. aygulus* (table 5). It was not difficult to achieve a model s' close to the measured value in *O. westermanni*, although the f' is a little high (f', measured from image size, is likely to be less accurate than s'). In the other two species, the agreement is acceptable but not as good as in *O. westermanni*, probably because we modelled the aspheric back surface of the cornea as hemispheric. There is significant refraction at this surface when the cornea is in saline, but much less *in situ* (see Methods). The main difference between the corneal lenses of *O. westermanni* and *O. alexis* is the tighter back-surface curvature in *O. alexis*.

The refractive power of the second component of the telescope, the proximal part of the crystalline cone, comes almost entirely from the refractive-index gradient, there being little refraction at the proximal end of the cone (refractive-index drop 0.01). The maximum and minimum values of the refractive index in the proximal cone are much the same for all three species (figure 12), but the shape of the gradient in *O. alexis* ($\alpha = 2.5$–2.75) and *O. aygulus* ($\alpha = 2.6$–2.75) differs significantly from that in *O. westermanni* ($\alpha = 1.9$–2.0).

The model *O. westermanni* ommatidium performs well (figure 14). At all angles up to the maximum (about 18°), the beam (beam direction is the mean direction of the emerging rays) in the two-dimensional ray traces emerges at an angle 1.6–1.7 times the incident angle. The spot diagrams, from three-dimensional ray traces, show that the beam spread is sufficiently small to form a small patch of light on the retina, about the size of a rhabdom.

In *O. alexis* (figure 15), there is a greater spread of light on the retina from each of the ommatidia, partly due to a greater angular spread in the beam than in *O. westermanni*, and partly due to the fact that the clear zone is wider in *O. alexis*. Because of this, the beam in *O. alexis* would have to have a smaller angular spread than in *O. westermanni* to achieve the same spread on the retina.

This effect is even more obvious in the plots for *O. aygulus* (figure 16), which has the widest clear zone of the three (table 3). However, the angular spread in the beam is also greater at large angles in *O. aygulus* than in the other two models.

Table 6 gives the mean angular magnification M and the spread in ray angles (beam spread) for each of the model ommatidia shown in figures 14–16. M remains approximately constant across the whole range of incident angles, as is necessary for a good superposition image to be formed in a spherically symmetrical eye. Although the model values do not exactly match the values M_0 predicted from eye geometry (table 3), the agreement is good.

TABLE 6. MEAN ANGULAR MAGNIFICATION M AND SPREAD $\Delta\beta$ OF RAYS FROM TWO-DIMENSIONAL RAY TRACES THROUGH THE MODEL OMMATIDIA AT DIFFERENT ANGLES OF INCIDENCE, AS IN FIGURES 14–16

(If $\bar{\beta}$ is the mean angle to the axis of the rays emerging from the proximal cone tip of an ommatidium, M is $\bar{\beta}$ divided by the angle of incidence and $\Delta\beta$ is the standard deviation in degrees about $\bar{\beta}$. Only those rays passing through the curved part of the distal crystalline-cone surface are included in $\bar{\beta}$. M at 0° is the paraxial angular magnification (table 7).)

angle	*O. westermanni*		*O. alexis*		*O. aygulus*	
deg	M	$\Delta\beta$°	M	$\Delta\beta$°	M	$\Delta\beta$°
0	1.5	0.2	1.1	1.5	0.9	1.1
5	1.6	0.4	1.2	0.5	1.0	0.6
10	1.7	0.5	1.3	1.5	1.1	1.5
15	1.7	0.4	1.3	2.5	1.1	3.5
20	—	—	1.2	1.2	1.0	3.2

PHILOSOPHICAL TRANSACTIONS OF THE ROYAL SOCIETY B BIOLOGICAL SCIENCES

(ii) *The superposition image*

Consideration of the superposition image formed by an entire eye shows that M_0 is in fact not the best value for M. This is because of the inherent spherical aberration of the spherically symmetrical eye. If a parallel beam of light (parallel incident rays) falls upon the eye, rays passing through ommatidia close to the central one (paraxial rays) are brought to a focus (cross the axis of the central ommatidium) proximal to those rays entering through more peripheral ommatidia (Land *et al.* 1979; Bryceson & McIntyre 1983). This leads to a blurring out of the focus along the axis of the central ommatidium, with the best focus lying somewhere between the paraxial focus (corresponding to a magnification M_0) and the more distal marginal focus. Aberrations of the ommatidial lenses compound this effect. Exactly what value of M is needed to place this best image on the distal rhabdom tips cannot be calculated without a detailed knowledge of the light distribution about the focus. Evidently though, it must be smaller than M_0.

A more direct way of relating optics and eye geometry is to trace rays (in three dimensions) through each of the ommatidia aligned as in the eye and project all emerging rays across the clear zone to form a superposition image. A two-dimensional ray trace was carried out for the eye of *Ephestia* by Cleary *et al.* (1977). Figures 17–19 show the superposition image of a point source at infinity (parallel incident rays) formed by the model eye of each of the three species considered here. The approximate outlines of several rhabdoms (traced from an eye section) are also shown, so that the spread in the image can be related to the structures that sample the image. The pattern of light intensity is shown as a spot diagram at the distance across the clear zone that gives the best image.

The model for *O. westermanni* corresponds closely to the actual eye and works very well as can be seen in figure 17. All of the rays that emerge from a total of 109 ommatidia are printed here; the bulk of these rays fall upon one rhabdom. This model is based upon the dimensions of specimen (1) of table 3, and the position of the best focus, 166 μm across the clear zone, agrees very well with the measured width of the clear zone in the central region of the eye.

The superposition image of the point source formed in *O. alexis* (figure 18) is not nearly as crisp as that of *O. westermanni*, but is still quite reasonable. The best image lies about 265 μm across the clear zone, close to the level of the distal tips of the rhabdoms. Two of the reasons for the larger scatter, the larger beam spread and wider clear zone, are discussed above; a third reason is that there are more ommatidia (241) contributing to the image. All of these contribute rays to a central region of the same diameter as the rhabdom. With this wider pupil, the aberrations are more pronounced and hence the image more blurred. Only rays passing through the curved central region of the distal surfaces of the cones are included in figure 18 so as to eliminate the artefactual refraction of the model (see Discussion). Presumably in a more accurate model of this region, the remaining rays would also contribute to the central part of the superposition image. This small discrepancy aside, the model is a reasonably accurate representation of the actual eye.

Much the same comments apply to the image formed by *O. aygulus* (figure 19). Here the number of contributing ommatidia is even larger at 637, 595 of which contribute rays to a central region of the same diameter as the rhabdom. If rays passing through the flat part of the distal cone surface are included, 673 ommatidia contribute, but with the present model, only 24 of the 594 rays from these extra ommatidia would appear on the spot diagram of

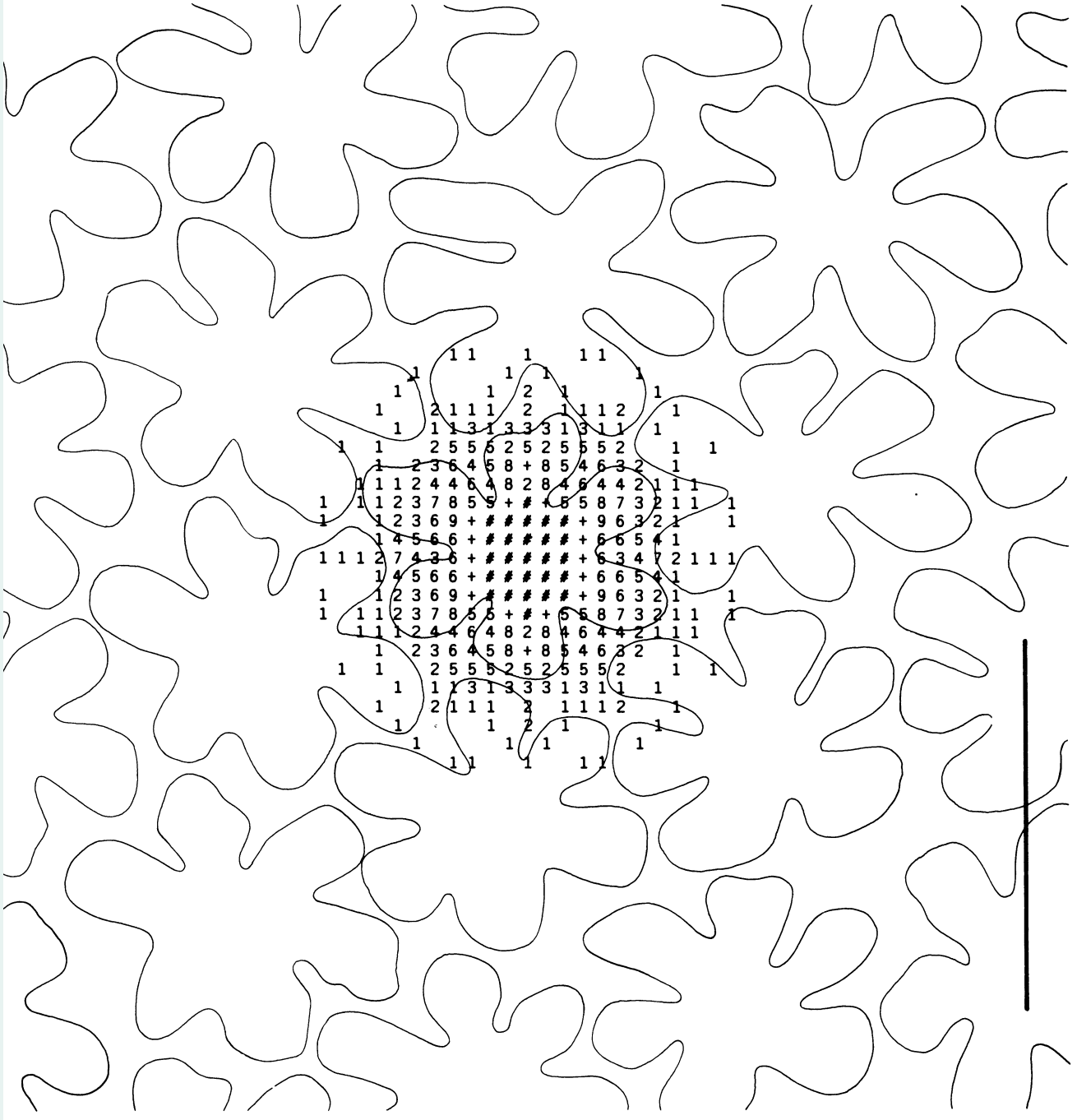

FIGURE 17. Superposition image of a distant point source formed by a model *O. westermanni* eye. The outlines of rhabdoms, taken from a section like that of figure 8, are also shown. +, 10–19 rays; ♯ over 19 rays. Scale bar 20 μm. Interommatidial angle 3°, radius of curvature of outer surface of the eye 600 μm. Best image 166 μm across the clear zone. 109 ommatidia contribute to the image and all contribute rays to a central region of diameter 15.5 μm (the maximum rhabdom diameter).

PHILOSOPHICAL TRANSACTIONS OF THE ROYAL SOCIETY B BIOLOGICAL SCIENCES

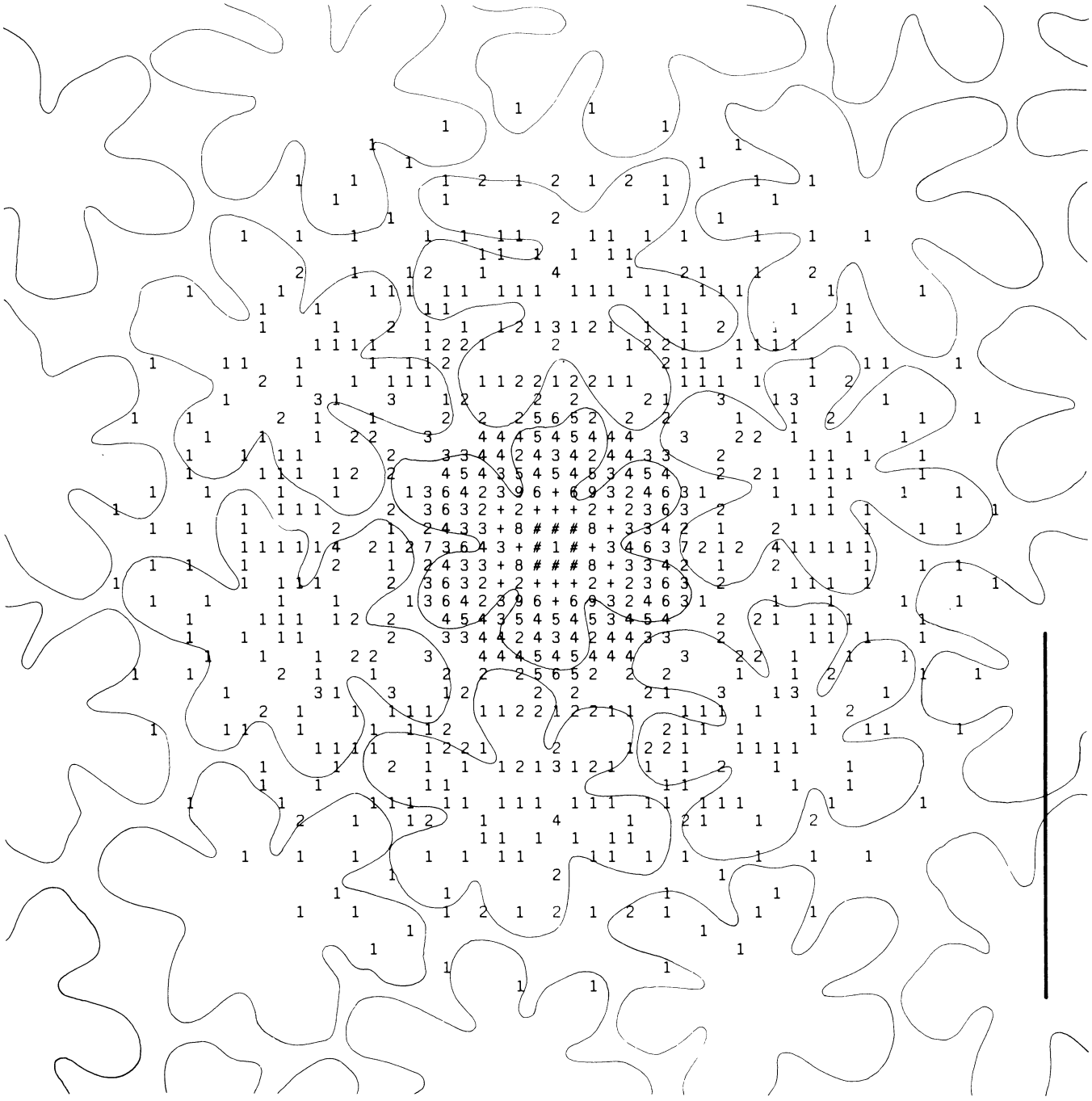

FIGURE 18. As for figure 17, but with model *O. alexis* eye. Interommatidial angle 2.5°, radius of curvature of outer surface of eye 750 μm. Best image 265 μm across the clear zone. 241 ommatidia contribute to the image, all of them to a central region 14 μm in diameter.

PHILOSOPHICAL TRANSACTIONS OF THE ROYAL SOCIETY B BIOLOGICAL SCIENCES

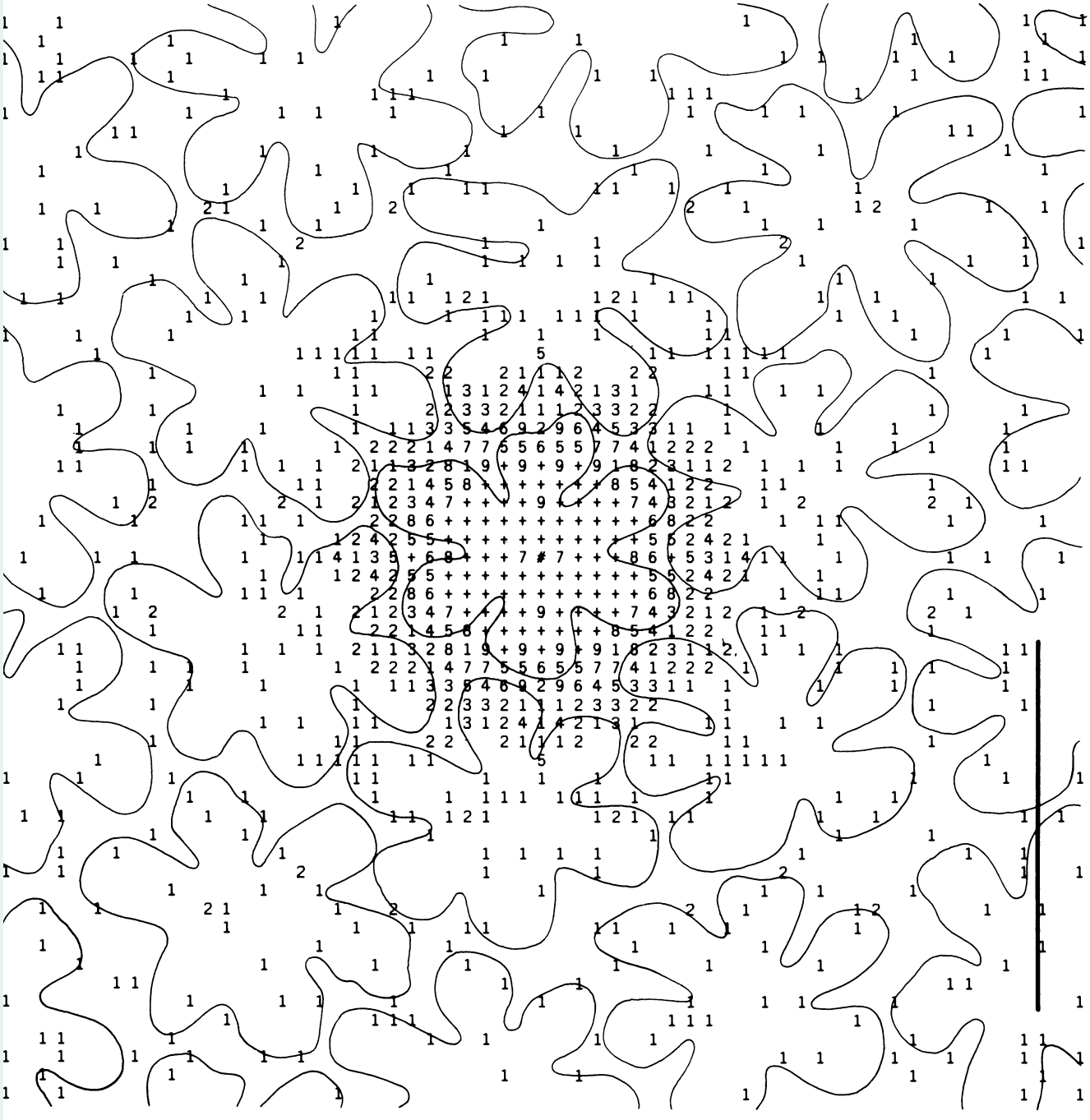

FIGURE 19. As for figure 17, but with model *O. aygulus* eye. Interommatidial angle 2°, radius of curvature of outer surface of eye 1000 μm. Best image 433 μm across the clear zone. 637 ommatidia contribute to the image, 595 of them to a central region 13 μm in diameter.

PHILOSOPHICAL TRANSACTIONS OF THE ROYAL SOCIETY B BIOLOGICAL SCIENCES

figure 19. The position of best focus is about 433 μm across the clear zone, compared with a clear-zone width of about 445 μm (table 3).

(*f*) *Flight trials*

The three species studied here fly at dusk, with flight ceasing as darkness falls. We were particularly interested in seeing whether differences in eye design in these species might be correlated with the time of peak flight activity and the light level at which the flight terminated. Only *O. alexis* and *O. westermanni* were flown, as insufficient numbers of *O. aygulus* were available. A total of 170 laboratory-reared specimens of *O. westermanni*, kept for several weeks in natural light in a greenhouse, and 78 field-collected *O. alexis* were mixed together and allowed to burrow into the soil in the flight chamber during the mid-afternoon. At dusk, the beetles that flew were collected at 10 min intervals and counted. During the first evening a total of 61 *O. westermanni* and 49 *O. alexis* flew. At the end of the trial, the beetles were returned to the soil in the flight chamber and tested again the following evening. Weather conditions on the two days were similar; the sky at dusk was clear and there was little wind. During the second trial, 25 *O. westermanni* and 17 *O. alexis* flew. No attempt was made to determine whether individual beetles flew on both evenings. The data from the two trials were pooled and are plotted as cumulative percent of beetles flown in figure 20.

From these data it can be seen that *O. westermanni*, on average, both starts and stops flying earlier than *O. alexis*. Many *O. westermanni* flew in the late afternoon, before sunset, whereas *O. alexis* rarely flies before sunset (see also Houston & McIntyre 1985). On average

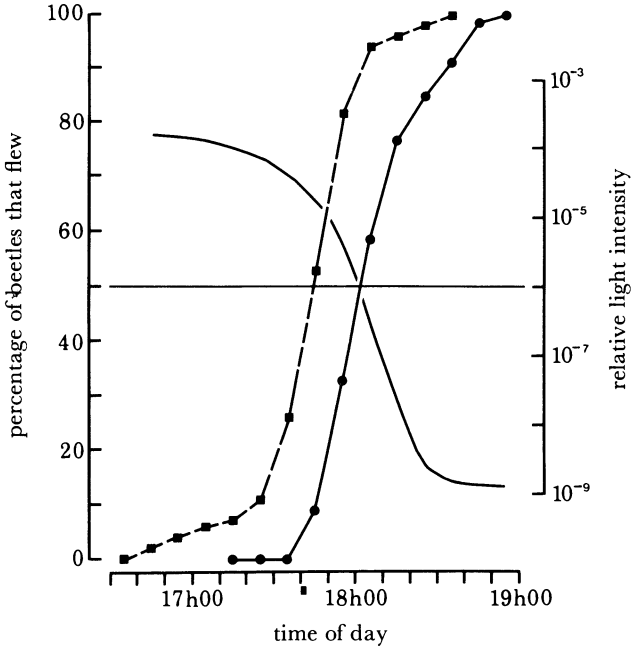

FIGURE 20. Time of onset of flight of *O. westermanni* (squares, dashed line) and *O. alexis* (circles). The (left-hand) ordinate shows cumulative numbers of beetles taking flight, expressed as a percentage of the total number that flew. The light intensity during the flight trials is shown by the solid curve that lacks symbols (logarithmic scale, right-hand ordinate). Recordings were made at 10 min intervals. The drop in light intensity ceased at about half-moon light (relative light intensity 1×10^{-9}). Local sunset (black square under the time scale) was at 17h42 and 17h40 on the consecutive evenings of the experiment. Soil temperature was maintained between 26 and 29 °C. Air temperature dropped from 26 to 21 °C.

O. westermanni flew 17 minutes earlier than *O. alexis*, the ambient light being about one order of magnitude brighter at this time. Furthermore, flight in *O. westermanni* stopped at about civil twilight (18h07 and 18h06 on these two evenings), whereas that of *O. alexis* extended further into the evening. The difference in the time at which 50% of the beetles had flown in the two species is exaggerated by the presence of early starters in *O. westermanni* (the initial shoulder in the curve) and late fliers in *O. alexis* (the slow trailing-off of flight activity in the curve). A more comprehensive study of flight activity in *O. alexis* (Houston & McIntyre 1985) suggests that although the light intensity at which 50% of *O. alexis* had flown is correct, the period of flight can be as short as 20 min and generally ends more abruptly than shown in figure 20.

4. Discussion

(*a*) *Features of the ommatidial lenses*

As shown in figures 14–16, the basic ommatidial optics in the three species are the same: the corneal lens and crystalline cone together form an afocal telescopic system with refractive power provided by the curved outer surface of the corneal facet and by g.r.i. lenses in the cornea and cone. The proximal part of the crystalline cone, which forms the second component (the 'eyepiece') of the telescope, is a particularly powerful g.r.i. lens, with a large drop in refractive index ($\Delta n = 0.11$–0.14: figure 12) over a distance of 10–12 μm between centre and edge. Although the proximal part of the cone has no significant refracting surfaces and a length one third to one half that of the first component (the corneal lens plus distal part of the cone), it has twice (*O. westermanni*) to 1.2 times (*O. aygulus*) the refractive power. The overall drop in refractive index in the proximal part of the cone is similar to that found in vertebrate lenses (Philipson 1969), but these are much bigger and consequently the gradient is much shallower.

Although the structure of the optical components in the three species is similar, there are significant differences in their optical properties, in particular in the angular magnification M and the maximum angle of incidence. These differences arise from differences in surface curvatures, principally that of the outer surface of the corneal facet, and in the refractive-index gradients in the crystalline cone. By adopting particular values for these parameters, the ommatidial lenses do three things:

(i) individually they direct a narrow, approximately collimated (parallel) beam of light onto the retina;

(ii) they set the maximum angle of incidence at which light can enter an ommatidium and still emerge from the proximal cone tip: this angle determines the aperture of the eye;

(iii) they set an angular magnification M which is approximately the same for all angles of incidence; among other things, this determines the overall size of the eye.

As the angle of incidence of a parallel beam of light on an ommatidium is increased, the intermediate image lies further and further from the cone axis (figures 14–16). The maximum angle of incidence occurs when the intermediate image reaches the side of the cone. Any further increase in angle will cause the image to fall outside the cone, where all the light will be absorbed by screening pigment surrounding the cone. Thus the maximum angle of incidence and hence the aperture of the eye are set by the diameter of the cone in the waist region, where the intermediate image falls, and by the refracting (ray-bending) properties of the first component of the telescopic system. The aperture of the eye is also related to the angular magnification M as shown in the next section.

PHILOSOPHICAL TRANSACTIONS OF THE ROYAL SOCIETY B BIOLOGICAL SCIENCES

The angular magnification M of an ommatidial lens is determined by the relative refractive powers of the two components. A weak first component (little refractive power) and a strong second component result in a large M, and the reverse situation in a small M. This idea can be formalized by considering paraxial rays, rays close to the axis of the ommatidium and at small angles to it. The angular magnification M_p for these rays is given by the ratio of the paraxial focal lengths of the two components, and these can be calculated from the model (table 7). To decrease angular magnification, the focal length of the first component must be decreased or the focal length of the second component increased. Table 7 shows that both of these occur, that is, following the sequence *O. westermanni*, *O. alexis*, *O. aygulus*, f_1' decreases, f_2 increases and consequently M_p decreases.

TABLE 7. PARAXIAL ANGULAR MAGNIFICATION M_p AND PARAXIAL FOCAL LENGTHS OF THE TWO COMPONENTS OF THE MODEL OMMATIDIAL LENSES (figures 14–16) OF THE THREE SPECIES

($M_p = f_1'/1.34f_2$ (Longhurst 1973), where f_1' is the back focal length of the first component, f_2 the front focal length of the second component and 1.34 the refractive index of the clear zone.)

	f_1'	f_2	M_p
O. westermanni	58.4	28.3	1.5
O. alexis	54.0	37.9	1.1
O. aygulus	46.1	39.7	0.9

The focal length is related to the angle which a ray, incident parallel to the axis (0° in figures 14–16), makes with the axis when it crosses it. This angle can be increased, and hence the focal length of a lens decreased, by moving the source of refractive power towards the back of the lens. If we consider the first component of the telescopic system, the corneal lens and distal part of the crystalline cone, this can be achieved by decreasing the curvature of the outer corneal surface and by increasing the length or power of the g.r.i. regions (figures 2, 5, 7, 14–16; Caveney & McIntyre 1981). In a g.r.i. lens, the smaller the exponent α, the larger the gradient seen by the paraxial rays and hence the shorter the paraxial focal length.

The decrease in the focal length of the first component is brought about initially (*O. westermanni* to *O. alexis*: figures 14 and 15) by an increase in the power of the g.r.i. regions in the proximal part of the cornea (steeper gradient because of smaller diameter) and in the distal part of the cone (longer g.r.i. region). A more significant decrease (*O. alexis* to *O. aygulus*: figures 15 and 16) results from a decrease in front-surface curvature (table 1) and a further increase in the power of the g.r.i. regions.

The larger difference in the focal lengths of the second components is between *O. westermanni* and *O. alexis* (table 7). This difference, an increase of about a third, is a result of the exponent α of the gradient in the cone increasing from 2 to 2.5 (figure 12), so that the paraxial rays see a shallower gradient. The second components of *O. alexis* and *O. aygulus*, which have similar values of α (figure 12), have similar focal lengths (table 7). Taken together with the changes in focal lengths of the first components, these differences result in a decrease in the paraxial angular magnification M_p from 1.5 in *O. westermanni* down via *O. alexis* (1.1) to 0.9 in *O. aygulus* (table 7).

So far we have considered only paraxial rays. However, if each ommatidial lens is to project a narrow beam of light across the clear zone at the correct angle, all rays, at angles up to as much as 30° to the axis, must be refracted correctly. This is done by having a refractive-index

gradient of the correct shape. For example in *O. aygulus*, the paraxial rays see only a slight gradient (figure 12), but rays at large angles to the axis see a very steep gradient. This refracts them strongly enough to keep them within the cone and to project them out of the proximal tip of the cone at an angle about equal to their angle of incidence (figure 16), as is the case with the paraxial rays. Although we have considered the two components of the ommatidial lens system in isolation in examining their refractive properties, they must of course be designed together. The angular magnification cannot, for example, simply be increased by increasing the exponent α of the cone gradient. Other adjustments must be made to ensure that all rays are still refracted correctly; presumably the aspheric proximal surface to the corneal lens associated with gradients in the cones for which α is greater than 2, as in *O. alexis* and *O. aygulus*, is just such an adjustment.

(*b*) *Image quality on the retina*

It is clear from our results that the superposition principle, as expounded by Exner (1891) does work and appears to work well, even when rays in three dimensions are included. Rays from most of the contributing ommatidia converge to form a good superposition image (figures 17–19), and for the eyes examined here, the best image formed by the model lies close to the retina. The blur circle, which is the superposition image of a distant point source, is comparable in size to a rhabdom in all three cases, and in the case of *O. westermanni*, almost all rays fall upon a single rhabdom (figure 17). We therefore conclude that the angular magnification M of the individual ommatidial lens systems is matched to the eye geometry and that the optics are such that a good superposition image is formed. Any significant deviation from the parameters used in the model results in a substantial degradation of the image on the retina.

Land *et al.* (1979) describe two possible arrangements of the geometry of refracting superposition eyes. One has the centre of curvature of the hemisphere on which the proximal cone tips lie, at the point of intersection of the ommatidial axes. This eye has equal vision in all directions, that is, no preferred direction, but suffers from a type of spherical aberration as described above. The retina is concentric with the cone-tip hemisphere. In the second arrangement, the radius of curvature of the cone-tip hemisphere is equal to half the distance between the proximal cone tips and the point of intersection of their axes. This arrangement forms an aberration-free image for light incident from one direction only, that is, has a preferred direction, but suffers from aberrations for light incident from other directions. For the best image to fall upon the retina at all angles of incidence, the retina must be flat, and consequently this eye has a restricted overall field of view compared with the first, all-round eye.

In our model eyes, we have assumed the first arrangement, but it is evident, especially in *O. westermanni* (figure 9), that there is some tendency in the direction of the second. The centre of curvature of the cone-tip hemisphere lies distal to the intersection of the ommatidial axes and the retina is slightly flatter than hemispheric. Facet tilt at the margins of the eye (figure 9) will also contribute to this tendency. It appears that *O. westermanni*, at least, has a foveal region, in the sense of slightly improved image quality for light incident from directions in which ommatidia in the centre of the eye are pointing. This is at the expense of image quality at the margins of the eye.

An alternative method of reducing the aberrations while still maintaining an all-round eye would be to have ommatidial lenses in which M decreased as the angle of incidence α increased. The necessary variation of M with α is not difficult to calculate. However, as can be seen from

PHILOSOPHICAL TRANSACTIONS OF THE ROYAL SOCIETY B BIOLOGICAL SCIENCES

table 6, for α up to 15°, M increases with increasing α, and it is only at large angles ($\alpha > 15°$) that the variation with α resembles that required. Rays at large angles are the most aberrated, so that this may in fact be functional. Further investigation is required.

(*c*) *Sensitivity, image brightness and angular magnification*

In comparing the sensitivities of different eyes, a certain amount of caution must be exercised. The reasons for this are set out clearly in Land (1981). If we assume that the tasks performed by the visual systems to be compared are similar, a reasonable assumption in the case of the three beetle species considered here, an appropriate measure of sensitivity is the number of photons absorbed per receptor per unit of luminance in the visual field being imaged. This gives (Land 1981; Kirschfeld 1974)

$$S = (\pi/4)\,(A/f)^2\,A_{\mathrm{R}}(1-\mathrm{e}^{-kx}), \tag{3}$$

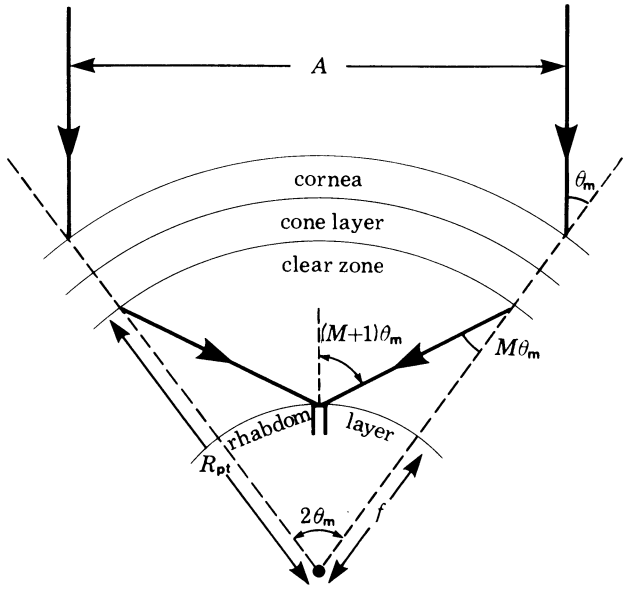

FIGURE 21. Geometry of the eye. The two extreme rays in an incident parallel beam are shown. A, the diameter of the aperture, is taken to be the distance between the axes of the extreme ommatidia as shown.

where S is sensitivity, A is the diameter of the aperture of the eye, f the posterior nodal distance (figure 21), A_{R} the cross-sectional area of the rhabdom, k the absorption coefficient of the rhabdom and x its length. The first term $(\pi/4)\,(A/f)^2$ gives the brightness of the retinal image of an extended source, A_{R} the amount of this light caught by a rhabdom and the last term, the fraction of this light actually absorbed by the rhabdom. The derivation of (3) assumes that all light incident on the eye reaches the retina. That this is not so is shown by the ray plots (figures 14–16) with large angles of incidence. Some light will be lost especially in the peripheral ommatidia in the aperture. Equation (3) therefore overestimates sensitivity somewhat, but should be reasonable for comparative purposes. Strictly speaking a weighting factor should be used to account for the different amounts of light transmitted by the lens systems of ommatidia in different parts of the aperture. An effective aperture could then be defined and used in (3).

The rhabdoms in the three species are irregular in cross-section (figure 8), but the shape is

the same in all three. We can therefore take $A_R = Ed^2$, where d is the maximum diameter and the constant E will be somewhat less than $\pi/4$, the value it would take if the rhabdoms were circular in cross-section. We can therefore write the sensitivity as

$$S = C(A/f)^2 d^2(1-e^{-kx}), \quad (4)$$

where $C = (\pi/4)E$ is a constant. The aperture A is taken here to be formed by those facets contributing rays that pass through a central circle of diameter d, the maximum rhabdom diameter (table 3), at the position of best focus. This value, calculated in the computer program, automatically takes account of the rhabdom cross-sectional area (d^2) in (4). The sensitivity can then be written (apart from a constant factor) as the product of image brightness $B = (A/f)^2$, a quantity proportional to the amount of light actually reaching the central rhabdom, and an absorption term $1-e^{-kx}$.

Table 8 gives the relative sensitivities of the three species, calculated in this manner. The ordering according to sensitivity and to relative image brightness is the reverse of the ordering according to angular magnification. *O. westermanni* is the least sensitive, with *O. alexis* about 2.8 times and *O. aygulus* about 5.9 times as sensitive. The increase in sensitivity arises from an increased image brightness and from longer rhabdoms, which increase the amount of light absorbed. The decrease in rhabdom diameter tends to reduce sensitivity. The F numbers of the eyes (Land 1981) range from 1.2 down to 0.6.

Table 8. Sensitivity data

(Aperture A (in micrometres) is calculated from the model eye and incorporates the rhabdom cross-sectional area (see text), posterior nodal distance f (in micrometres) is taken from table 3. F-number $F = f/A$, relative image brightness $B = (A/f)^2 = 1/F^2$, normalized to give a value of 1 for *O. westermanni*. The final result, sensitivity S, is calculated by using values for x from table 3 and absorption coefficient $k = 0.0067\ \mu m^{-1}$ (Land 1981), and normalized to a value of 1 for *O. westermanni*.)

	A	f	F	rel B	rel S
O. westermanni	263	320	1.2	1	1
O. alexis	427	350	0.8	2.2	2.8
O. aygulus	749	430	0.6	4.5	5.9

It is clear that angular magnification and image brightness are related. This relationship can be made explicit by using the geometry of the eye and an empirical result from the model. From the geometry of a spherically symmetrical eye (figure 21), the aperture diameter A is given approximately by $A = 2R_{pt} \sin\theta_m$, where R_{pt} is the distance from the centre of curvature of the eye to the proximal tips of the cones (table 3), and θ_m is half the angle between the axes of the ommatidia at either end of a diameter of the aperture. θ_m is also the angle between parallel incident rays and the axis of an ommatidium at the edge of the aperture. Therefore image brightness $B = (A/f)^2$ is given by

$$B = [(2R_{pt} \sin\theta_m)/f]^2.$$

If eye geometry and angular magnification M are matched, as they must be to give the best image on the retina, R_{pt}, f and M are related approximately by $M = f/(R_{pt}-f)$ (table 3). Rearranging gives $R_{pt}/f = (M+1)/M$, so that

$$B = [(2(M+1) \sin\theta_m)/M]^2.$$

PHILOSOPHICAL TRANSACTIONS OF THE ROYAL SOCIETY B BIOLOGICAL SCIENCES

θ_m can be written in terms of M by making use of a result from the model. *The maximum angle of rays to an ommatidial axis after their emergence from the cone (of that ommatidium) is approximately the same in all three species at just under* 30° (27° in *O. aygulus*, 26° in *O. alexis*, 25° in *O. westermanni*). This can be shown in two ways. The angle of incidence is increased in the models of figures 14–16 until an angle is reached at which rays just emerge from the proximal tip of the cone, and the angle of the emerging rays to the ommatidial axis calculated. Alternatively, rays can be traced in the reverse direction, as in Caveney & McIntyre (1981). Rays incident on the proximal cone tip at angles just greater than those given above, hit the sides of the cone; rays incident in the usual direction could therefore not emerge at angles larger than these. The angle of just less than 30° represents the maximum bending power of the proximal-cone-tip g.r.i. lens, and the value depends, as might be expected, almost entirely on the maximum refractive-index difference in the gradient. As this is the same for all three species (figure 12), the maximum angle of emergence is the same. 30° is also the maximum value found by Land *et al.* (1979) in the eyes of euphausiids. The maximum angle of emergence is $M\theta_m$, as θ_m is the maximum angle of incidence and M the angular magnification of the ommatidial lens (figure 21). Therefore we set $M\theta_m = 30°$, giving $\theta_m = 30°/M$, and finally

$$B = \{[2(M+1)\sin(30°/M)]/M\}^2,$$

a function of M alone. Image brightness given by this equation is shown in figure 22. This curve provides the link between the optical properties of the individual ommatidial lenses and the brightness of the superposition image formed by them. If the maximum angle of emergence is an angle other than 30° (different refractive-index values), the shape of this curve remains the same, but it is displaced slightly to the left or right of the 30° curve.

Also shown in figure 22 is the relative eye size R_{pt}/f as a function of M. Given the radius of curvature f of the rhabdom layer, this ratio sets the overall size of the eye. The clear-zone width is $R_{pt} - f$. This second curve also gives the maximum angle between the axis of a rhabdom and rays entering it ($(M+1)\theta_m$: figure 21) in multiples of 30°.

As an example using figure 22, an eye with $M = 2$ will have an image brightness of 0.6, a relative eye size of 1.5, a clear-zone width of $0.5f$ and rays entering the rhabdoms at angles up to 45° to their axes. If M is decreased to 1 (and the eye geometry altered accordingly), the image will be 6.7 times brighter ($B = 4.0$), but the eye 1.2 times larger (assuming the same f) and rays will enter the rhabdoms at angles up to 60°. To achieve a brighter image, and hence a greater sensitivity, by a change in the optics alone requires a larger eye (see Land 1981) and the rhabdoms to trap light at larger angles. Thus by adopting a suitable M value and the appropriate eye geometry, an eye can set image brightness. For M greater than 2, significant changes in image brightness require large changes in M, whereas for M around 1, changes in image brightness with M are very rapid (figure 22). As M becomes large, the clear-zone width and the image brightness tend to zero, and the eye becomes an apposition eye.

In the three species considered here, the eyes are similar in structure, but the M values vary considerably and the eye geometry varies to match M. Thus the overall sensitivities are different, allowing each species to function most efficiently at different light levels and hence at slightly different periods at dusk. With the rapid decrease in light intensity at dusk, 10 min is roughly equivalent to 1 log unit (figure 20).

A problem arising from our optical results concerns the trapping of light by the rhabdoms. The optics of the eyes' optical systems appear to be capable of forming good images on the

PHILOSOPHICAL TRANSACTIONS OF THE ROYAL SOCIETY B BIOLOGICAL SCIENCES

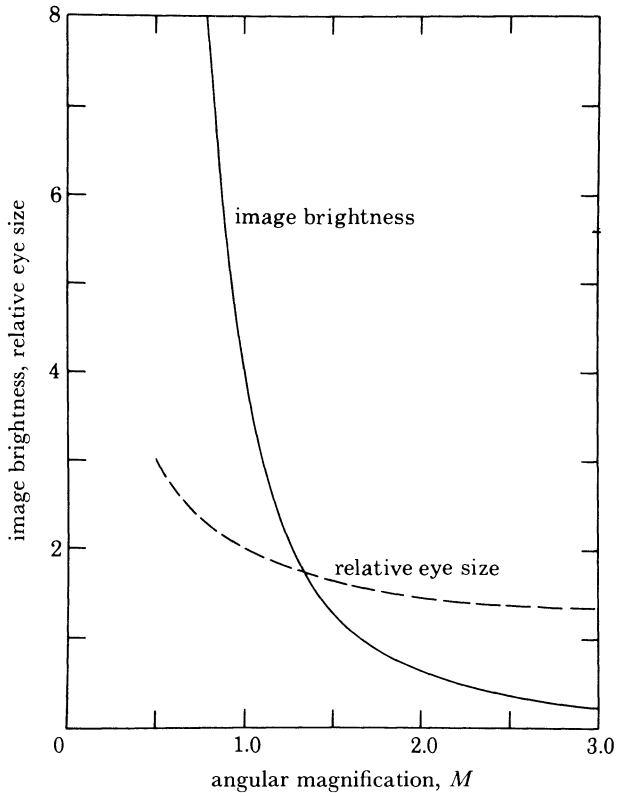

FIGURE 22. Image brightness $(A/f)^2$ and relative eye size R_{pt}/f as a function of the angular magnification M of the ommatidial lenses, assuming a maximum exit angle of 30°. The curve for relative eye size also gives the maximum angle at which light enters a rhabdom, as a multiple of the maximum exit angle; for example, at $M = 1$, this value is 2, so that light enters the rhabdom at up to 60° to its axis. Both curves are terminated at $M = 0.5$; at this value light enters the rhabdom at angles up to 90° to its axis.

retina, allowing good resolving power in principle. However, as shown above, many of the rays contributing to the image are incident on the rhabdoms at large angles to the rhabdom axis. Unless each ray can be trapped effectively in a single rhabdom, this good resolution will be degraded. The mechanism of total internal reflection can only trap rays at angles up to about 17° to the axis (refractive index of rhabdom 1.4, surround 1.34), so that some sort of reflecting layer isolating the individual rhabdoms (Land 1984) seems essential (an absorber would also work, but light would then be lost). These are present in some species (Gokan 1973), but have not been found so far in the three species considered here. It would appear strange however to throw away the excellent resolving power conveyed by the optics by not trapping light efficiently in the rhabdoms.

(*d*) *The relation of eye design to flight activity*

Clear-zone superposition eyes are found in beetles predominantly active at dusk or at night. Differences in the eye design of the three crepuscular species described here may be related to precisely when they fly at dusk: *O. westermanni*, with an eye of smaller superposition aperture and lower relative sensitivity (table 8) than that of *O. alexis*, on average both initiates and terminates its flight earlier during dusk.

Many day-active beetles also have clear-zone eyes, as Exner (1891) first noted in the flower

chafer *Cetonia*. In the majority of these beetles, the clear-zone superposition eye is converted into a clear-zone apposition eye at high light intensities by the formation of a light-shielded crystalline tract at the proximal tip of the crystalline cone (Gokan 1973; Meyer-Rochow & Horridge 1975), but superposition images are formed in some insect species in bright light, such as in the skipper butterfly (Horridge *et al.* 1972) and the day-flying moth *Phalaenoides* (Horridge *et al.* 1977). Here no changes in cell shape occur during dark–light adaptation.

The diurnal superposition eye is also found in several taxa of scarab beetles. Crystalline tracts form in the clear-zone eyes of all crepuscular leaf chafers (Rutelinae, Melolonthinae) in bright light (Gokan 1973; Meyer-Rochow & Horridge 1975), but are absent from the eyes of the two most advanced scarab subfamilies, the scarabaeine dung beetles (Meyer-Rochow 1978) and the cetoniine flower chafers (Gokan 1973). The flower chafers are exclusively day-active, but many genera of the dung beetles possess both diurnal and crepuscular or nocturnal species (Caveney & McIntyre 1981).

The clear-zone in the superposition eye of many diurnal dung beetles is narrower relative to eye geometry, and the lens elements proportionally closer to the retina, than in dung beetles active at dusk or night. For good superposition images to fall on the retina in day-flying species, the angular magnification of the ommatidial lenses must be greater than that in the eyes of the nocturno-crepuscular species reported in this paper. Higher angular magnifications than those reported here are probably achieved by further exaggeration of the optical differences in the lenses of *O. westermanni* compared to *O. aygulus*. Indeed, the cornea is generally thicker, and the crystalline cone generally shorter, in diurnal scarab species (Gokan 1973). We have just begun to examine the eye of a day-flying species, *O. belial*. The clear-zone is narrow and M would have to be slightly greater than 2 for the superposition image to fall on the distal surface of the retina. The thick cornea is strongly faceted and the crystalline cone is small in this species, suggesting that the angular magnification is high. Preliminary modelling gives about the right angular magnification and a good focus on the distal rhabdom. We now plan a complete analysis of several day-flying species by using the methods described in this paper.

(*e*) *The model*

Of necessity there are a number of approximations made in the model; here we give an outline of some of these. We have divided the corneal lens into three distinct regions, the first homogeneous and the others g.r.i. regions, characterized by the gradient slope α. The actual corneal lenses do have an outer homogeneous region and a g.r.i. region (figure 10); the approximation lies in having a distinct boundary in the model. The gradient actually builds up (α decreases from a large number to 2) quite rapidly but still over a few micrometres (figure 10).

In the model, the back surface of the corneal lens is taken to be hemispherical, a good approximation for *O. westermanni* (figure 7), but less realistic in *O. alexis* and *O. aygulus*, both of which have aspherical back corneal surfaces (figures 2 and 5). Where the cornea is inserted into the cone, the shape of the surface is of little consequence because the refractions at the back corneal surface and the distal cone surface tend to cancel. However for rays incident on the back corneal surface at its margins, this is not the case. These rays are incident at quite large angles to the surface and after refraction, pass through the flat part of the distal surface of the model cone. Often these rays emerge at quite different angles to the main body of rays as can be seen to a small extent in figure 14. This is particularly a problem with skew rays.

PHILOSOPHICAL TRANSACTIONS OF THE ROYAL SOCIETY B BIOLOGICAL SCIENCES

It was partly to minimize this artefactual refraction in the model that the refractive index of the region between cornea and cone was chosen to be 1.38, significantly higher than that of the clear zone. This region does however appear to be denser than the clear zone. In the three-dimensional plots for *O. alexis* and *O. aygulus* (figures 15, 16, 18 and 19), only rays passing across the curved part of the distal cone surface are included.

The corneal gradient is difficult to measure precisely and for this reason, the back focal distance and back focal length of the corneal lens alone (in saline) were also measured (Caveney & McIntyre 1981). The dimensions of the various regions in the corneal model were then adjusted so that the model cornea gave values close to those measured. One problem with this method is that in saline, refraction at the back corneal surface is much greater than with the cone in place; errors in modelling this surface can therefore lead to significant errors in the values of s', f' from the model corneal lenses, but this is of less significance in the full model.

In the cone, the exponent α of the gradient decreases as we go proximally (figure 12). In the model, only one value of α is used: this was chosen to be that in the waist–proximal-tip region so that the powerful lens formed by the proximal part of the cone was modelled accurately. The gradient at the distal end of the cone (concentric with the distal surface) was modelled as a homogeneous region with refractive index n_{0c} (figure 13). This appears to be a good approximation to the actual situation but remains to be tested properly. The length of the homogeneous region was adjusted within a small range to fine tune the model. Presumably if good results can be achieved with our approximate model, a real eye with more sophisticated optics can do as well, if not better.

Much of this work was done while the authors were Visiting Fellows at the Australian National University.

Professors Adrian Horridge (A.N.U.) and John Burns (Duntroon) provided research space and facilities.

We are deeply indebted to Dr Keith Houston of the Division of Entomology, C.S.I.R.O., who both reared and field-collected beetles, as well as advised us on the design of the flight trials.

Tim McIntyre was responsible for much of the computer programming and Brent Steer provided excellent technical assistance in histology. Dr Stan Meggitt kindly gave us his ray-tracing program. Dr Mike Land and Dr Dan-Eric Nilsson read the manuscript and contributed many useful comments.

This work was partly funded by the Natural Sciences and Engineering Research Council of Canada through an International Collaborative Research Grant to S.C. and by the Australian Research Grants Scheme through a grant to P.M.

REFERENCES

Bryceson, K. P. & McIntyre, P. 1983 Image quality and acceptance angle in a reflecting superposition eye. *J. comp. Physiol.* A **151**, 367–380.

Caveney, S. & McIntyre, P. 1981 Design of graded-index lenses in the superposition eyes of scarab beetles. *Phil. Trans. R. Soc. Lond.* B **294**, 589–632.

Cleary, P., Deichsel, G. & Kunze, P. 1977 The superposition image in the eye of *Ephestia kühniella*. *J. comp. Physiol.* **119**, 73–84.

Exner, S. 1891 *Die Physiologie der facettirten Augen von Krebsen und Insecten.* Leipzig and Vienna: Franz Deuticke.

Fletcher, A., Murphy, T. & Young, A. 1954 Solutions of two optical problems. *Proc. R. Soc. Lond.* A **223**, 216–225.

PHILOSOPHICAL TRANSACTIONS OF THE ROYAL SOCIETY B BIOLOGICAL SCIENCES

Gokan, N. 1973 The compound eye of the lamellicera leaf-chafers and the relation between their structure and activities. *Kontyu Tokyo* **41**, 106–125.

Gokan, N. 1982 Fine structure of the compound eyes of scarabaeid beetles. In *The ultrastructure and functioning of insect cells* (ed. H. Akai, R. C. King & S. Morohoshi), pp. 117–120. Tokyo: Society for Insect Cells.

Hausen, K. 1973 Die Brechungsindices im Kristallkegel der Mehlmotte *Ephestia kühniella*. *J. comp. Physiol.* **82**, 365–378.

Horridge, G. A., Giddings, C. & Stange, G. 1972 The superposition eye of skipper butterflies. *Proc. R. Soc. Lond.* B **182**, 457–495.

Horridge, G. A., McLean, M., Stange, G. & Lillywhite, P. G. 1977 A diurnal moth superposition eye with high resolution *Phalaenoides tristifica* (Agaristidae). *Proc. R. Soc. Lond.* B **196**, 233–250.

Houston, W. W. K., Feehan, J. E. & Runko, S. 1982 Methods for harvesting large numbers of dung beetles (Coleoptera: Scarabaeidae). *J. Aust. Ent. Soc.* **21**, 217–219.

Houston, W. W. K. & McIntyre, P. 1985 The daily onset of flight in the crepuscular dung beetle *Onitis alexis* (Coleoptera: Scarabaeidae). *Entomol. exp. appl.* (In the press.)

Kirschfeld, K. 1974 The absolute sensitivity of lens and compound eyes. *Z. Naturforsch.* **29**c, 592–596.

Kunze, P. 1979 Apposition and superposition eyes. In *Vision in invertebrates*, *Handbook of sensory physiology*, vol. 7, pt 6A (ed. H. Autrum), pp. 441–502. Berlin: Springer-Verlag.

Land, M. F. 1981 Optics and vision in invertebrates. In *Vision in invertebrates*, *Handbook of sensory physiology*, vol. 7, pt 6B (ed. H. Autrum), pp. 471–592. Berlin: Springer-Verlag.

Land, M. F. 1984 The resolving power of diurnal superposition eyes measured with an ophthalmoscope. *J. comp. Physiol.* A **154**, 515–533.

Land, M. F. & Burton, F. A. 1979 The refractive index gradient in the crystalline cones of the eyes of a euphausiid crustacean. *J. exp. Biol.* **82**, 395–398.

Land, M. F., Burton, F. A. & Meyer-Rochow, V. B. 1979 The optical geometry of euphausiid eyes. *J. comp. Physiol.* **130**, 49–62.

Longhurst, R. S. 1973 *Geometrical and physical optics* (3rd edn). London: Longmans, Green.

Marchand, E. W. 1982 Gradient-index imaging optics today. *Appl. Opt.* **21**, 983.

Meggitt, S. M. A. & Meyer-Rochow, V. B. 1975 Two calculations on optically non-homogeneous lenses. In *The compound eye and vision of insects* (ed. G. A. Horridge), pp. 314–320. Oxford: Clarendon Press.

Meyer-Rochow, V. B. 1977 Structure and possible function of the unusual compound eye of *Sericesthis geminata* (Coleoptera: Scarabaeidae). *N.Z. Jl Zool.* **4**, 21–34.

Meyer-Rochow, V. B. 1978 Retina and dioptric apparatus of the dung beetle *Euoniticellus africanus*. *J. Insect Physiol.* **24**, 165–179.

Meyer-Rochow, V. B. & Horridge, G. A. 1975 The eye of *Anoplognathus* (Coleoptera: Scarabaeidae). *Proc. R. Soc. Lond.* B **188**, 1–30.

Nilsson, D.-E., Andersson, M., Hallberg, E. & McIntyre, P. 1983 A microinterferometric method for analysis of rotation-symmetric refractive-index gradients in intact objects. *J. Microsc.* **132**, 21–29.

Philipson, B. 1969 Distribution of protein within the normal rat lens. *Invest. Ophthal. Visual Sci.* **8**, 258–269.

Vogt, K. 1974 Optische Untersuchungen an der Cornea der Mehlmotte *Ephestia kühniella*. *J. comp. Physiol.* **88**, 201–216.

PHILOSOPHICAL TRANSACTIONS OF THE ROYAL SOCIETY B BIOLOGICAL SCIENCES

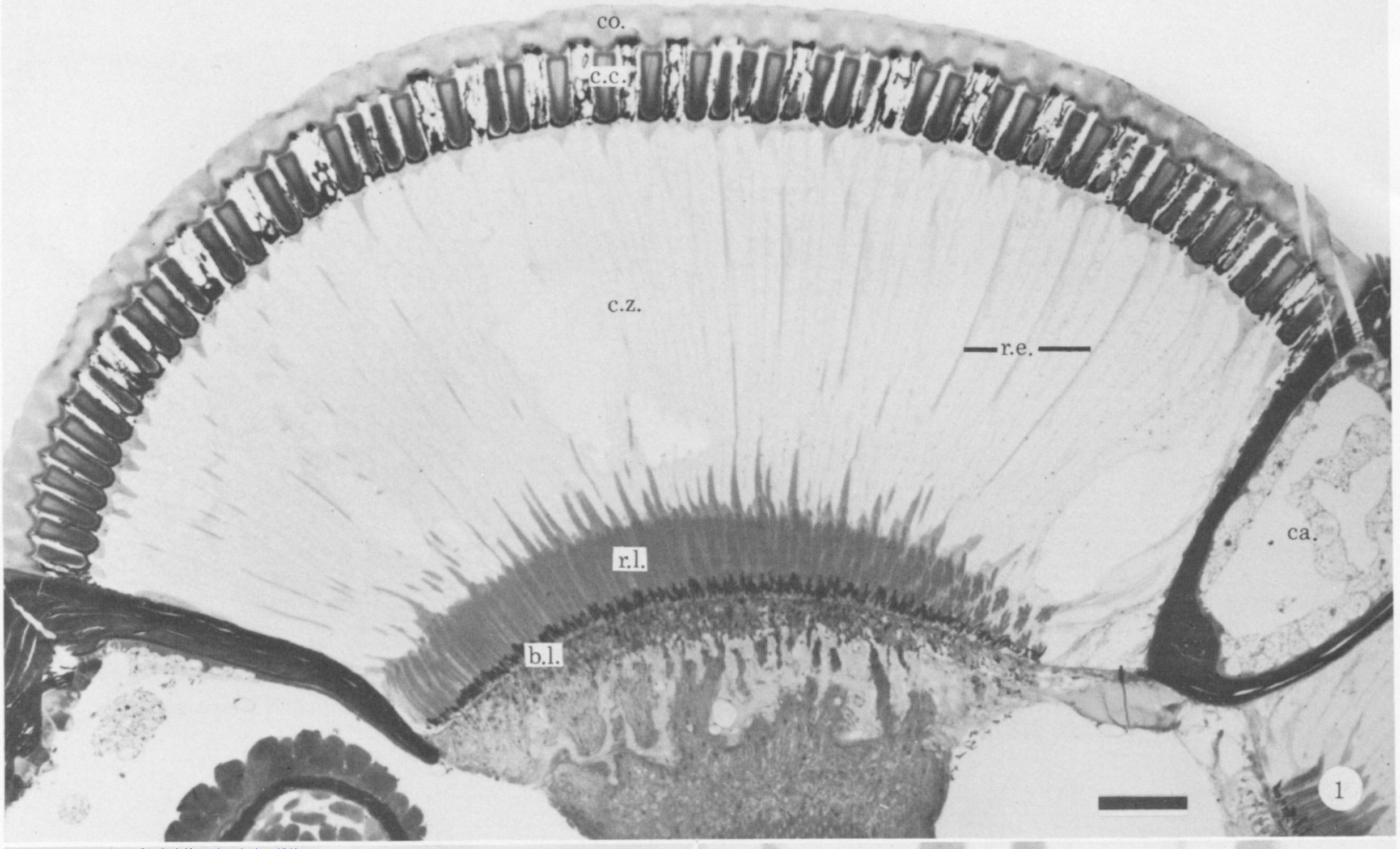

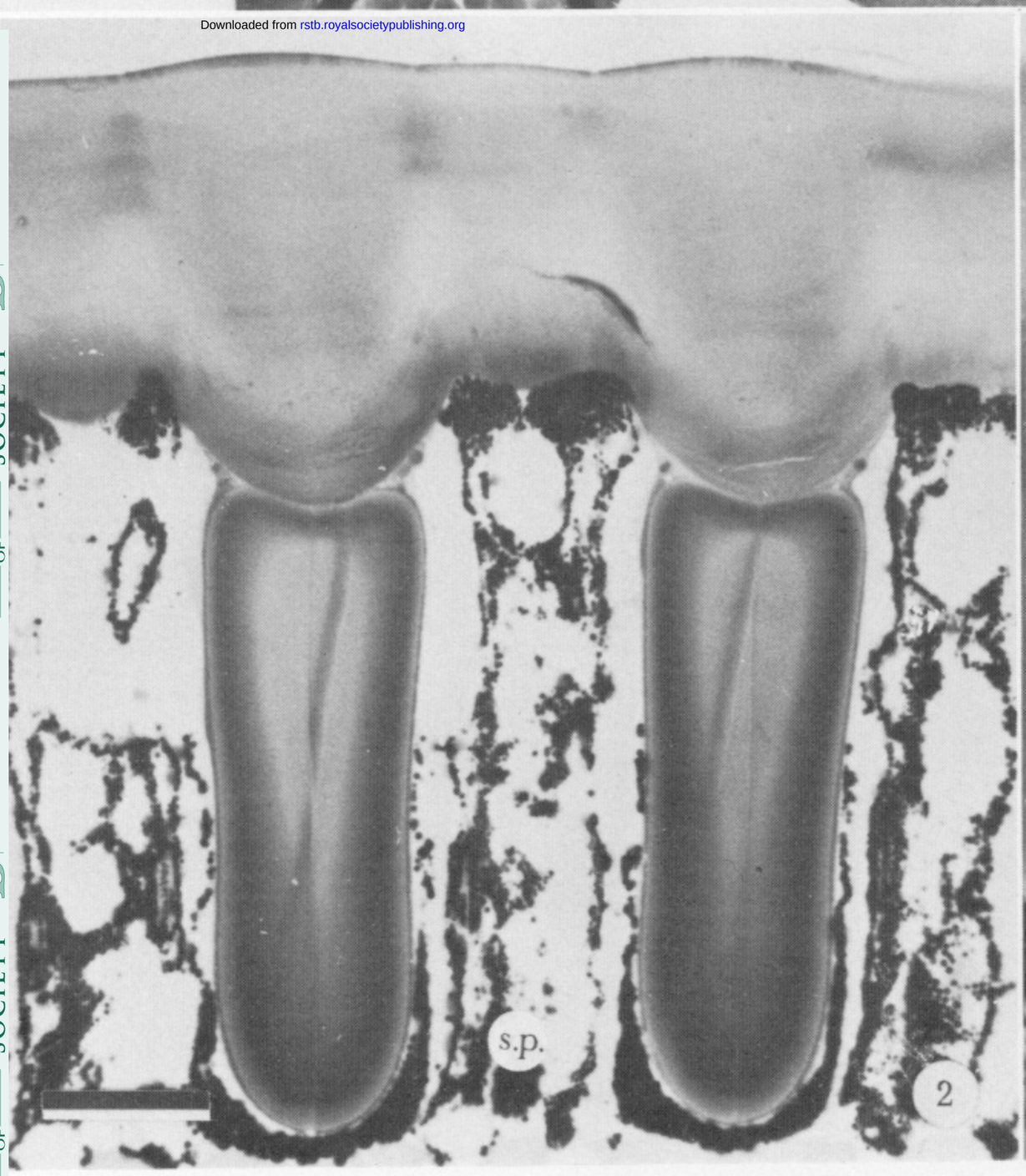

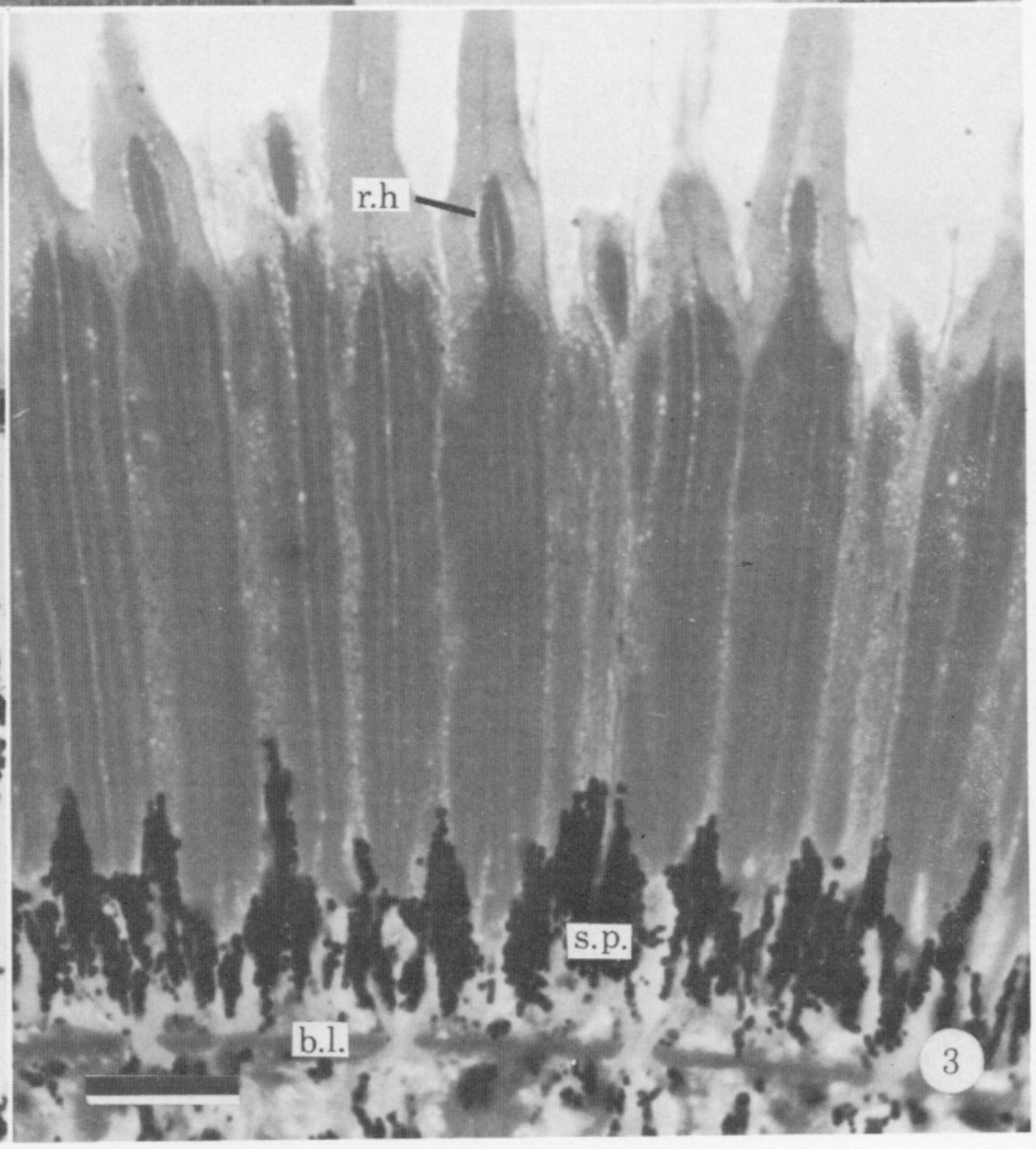

FIGURES 1–3. For description see opposite.

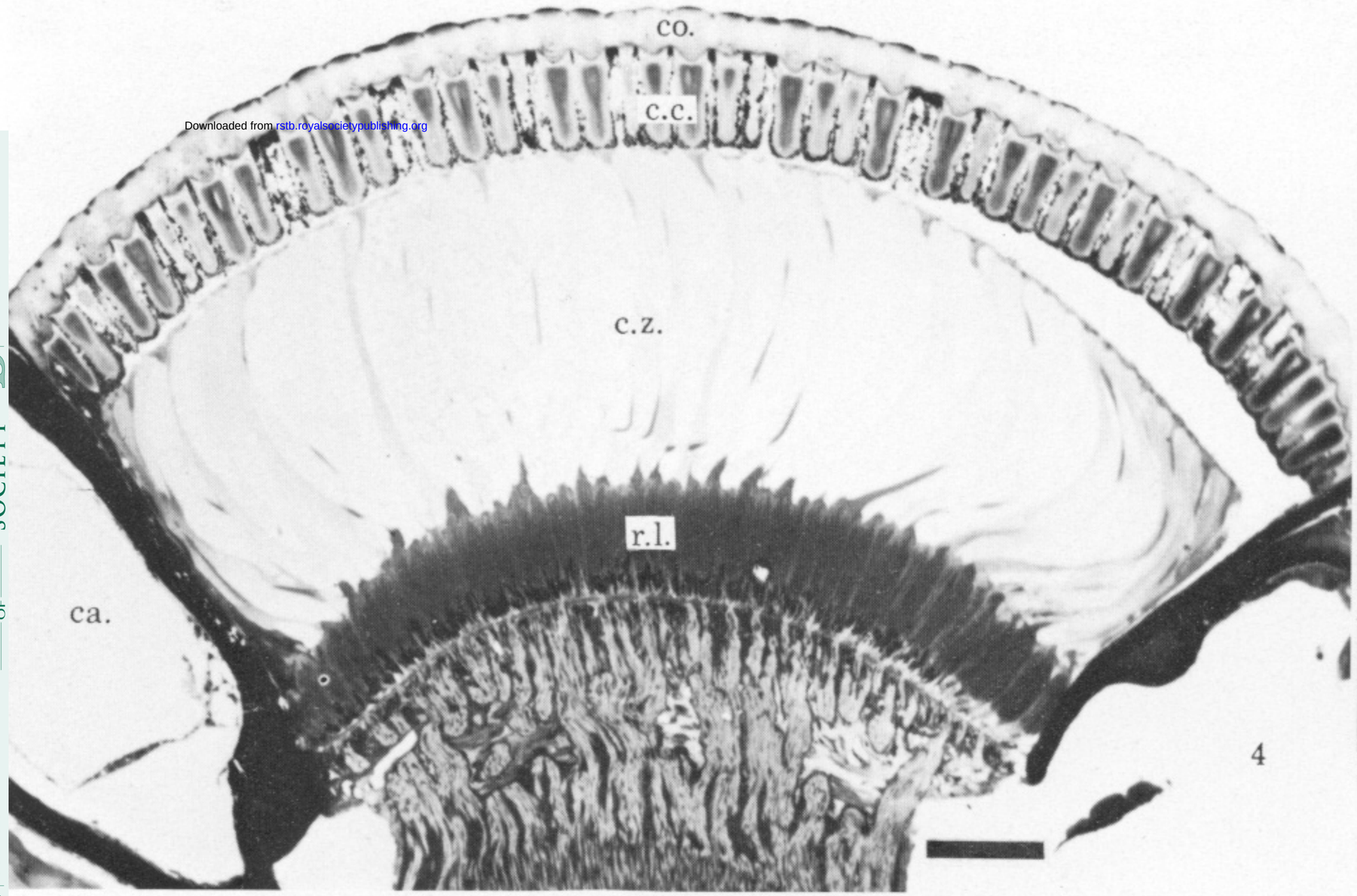

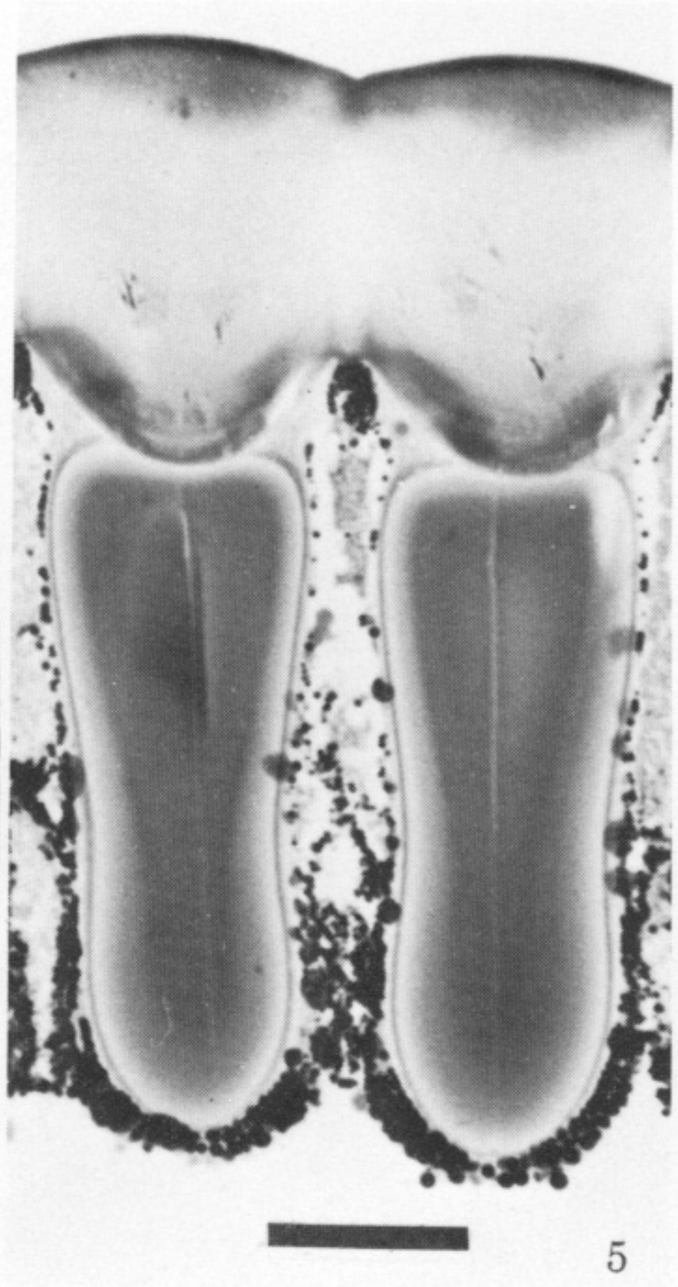

FIGURES 4 AND 5. Ventral compound eye of *O. alexis*. Abbreviations as in figures 1–3.

FIGURE 4. Section as in figure 1, at the same magnification, to show the relationship between the elements of the eye. The facets have a greater curvature in this species and the clear zone is proportionally thinner. The clear zone has partly separated from the cone layer during fixation. Scale bar 100 μm.

FIGURE 5. Corneal facets and crystalline cones cut longitudinally. The stronger facet curvature is clear in this micrograph, as is the looser insertion of the crystalline cones into the inner surface of the corneal facets. Scale bar 20 μm.

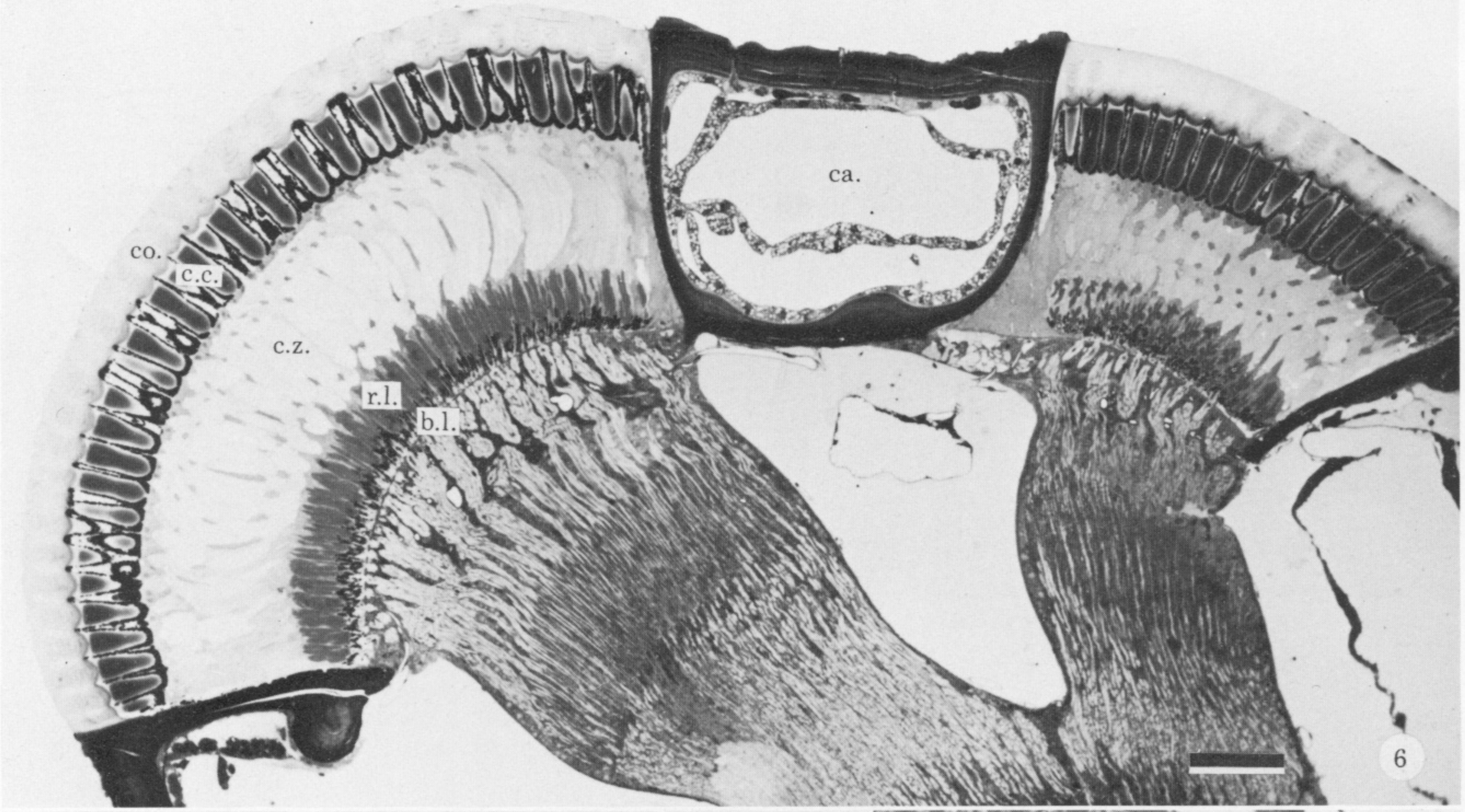

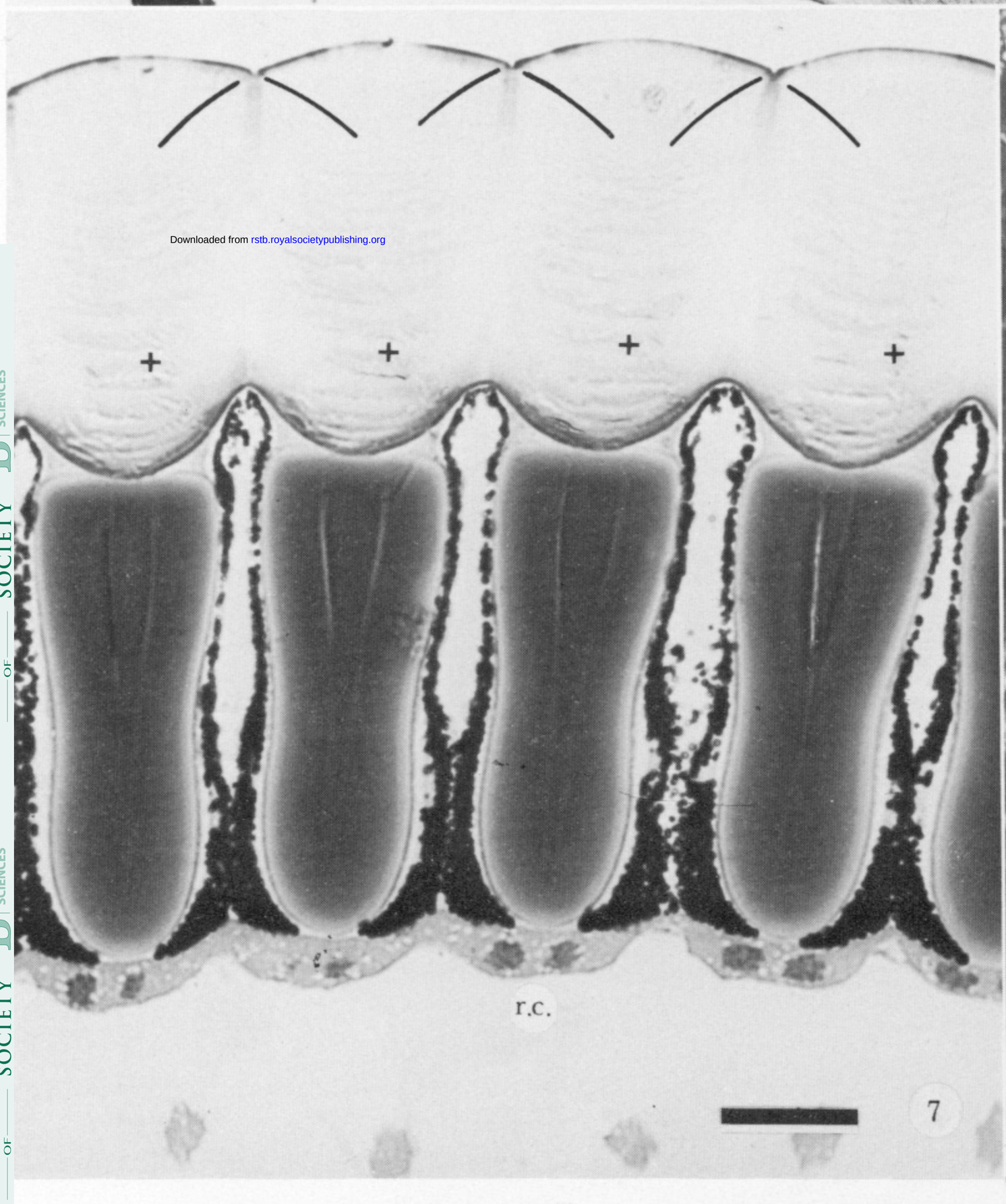

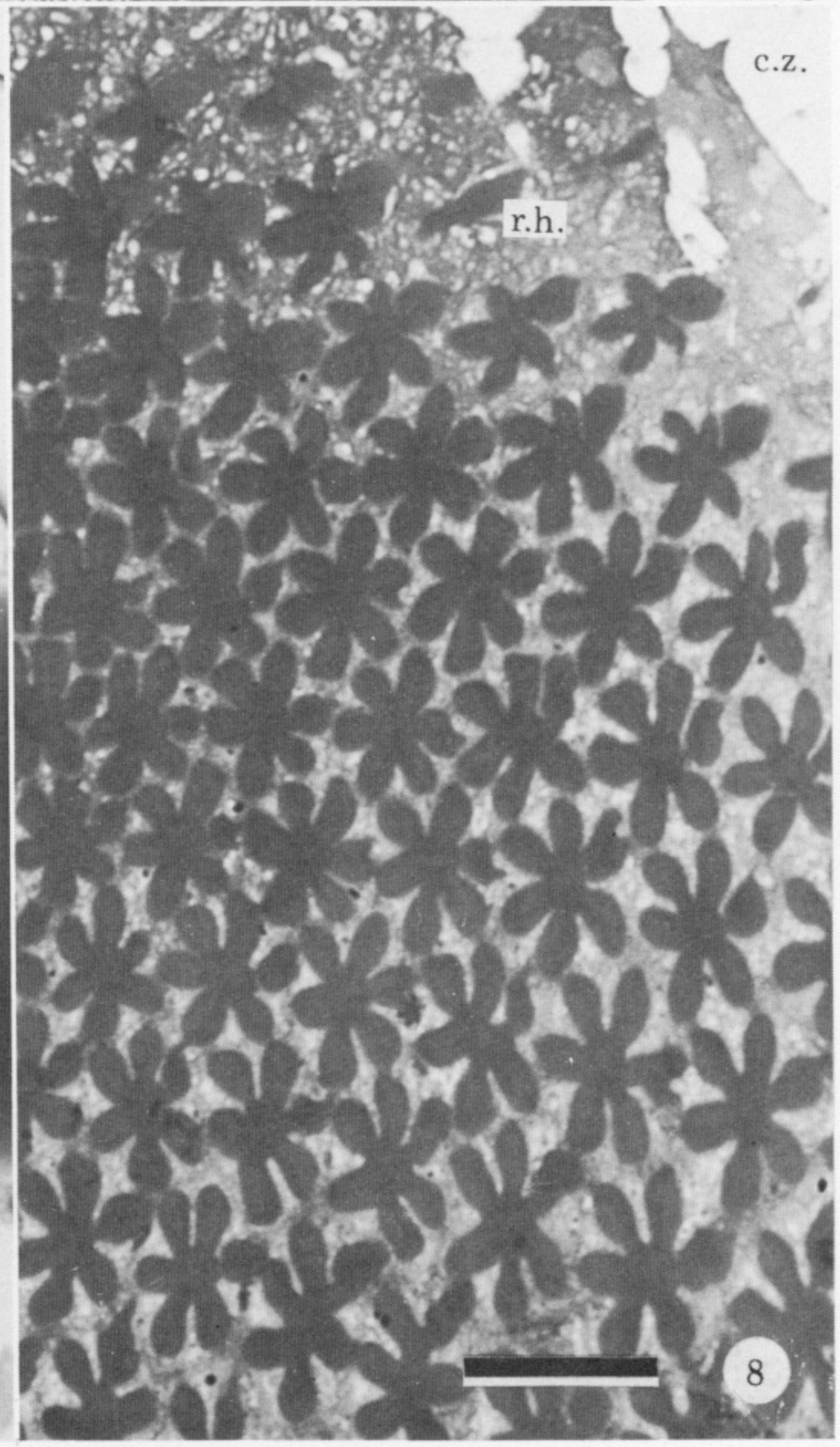

PHILOSOPHICAL TRANSACTIONS OF THE ROYAL SOCIETY B BIOLOGICAL SCIENCES

FIGURES 6–8. For description see opposite.

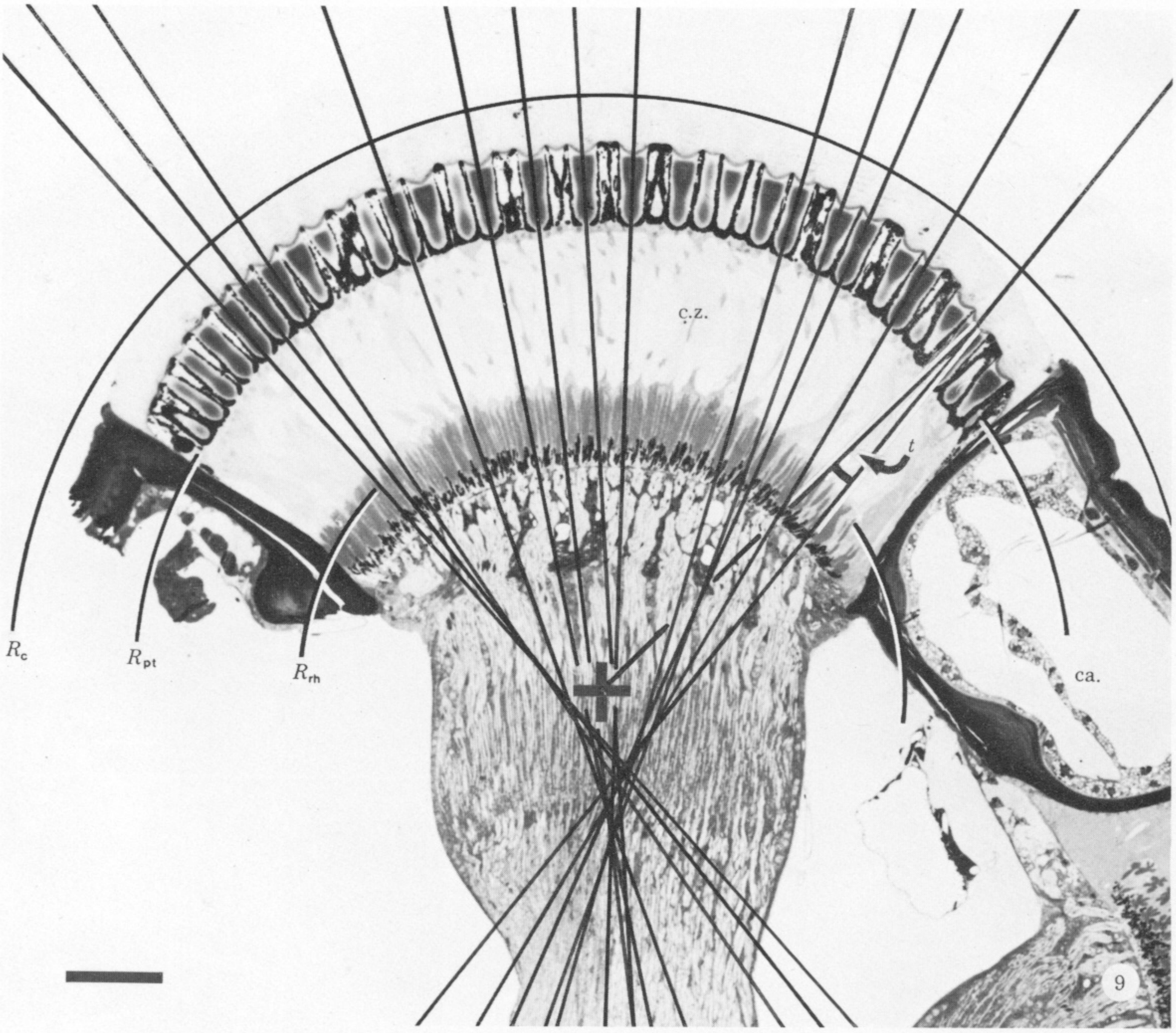

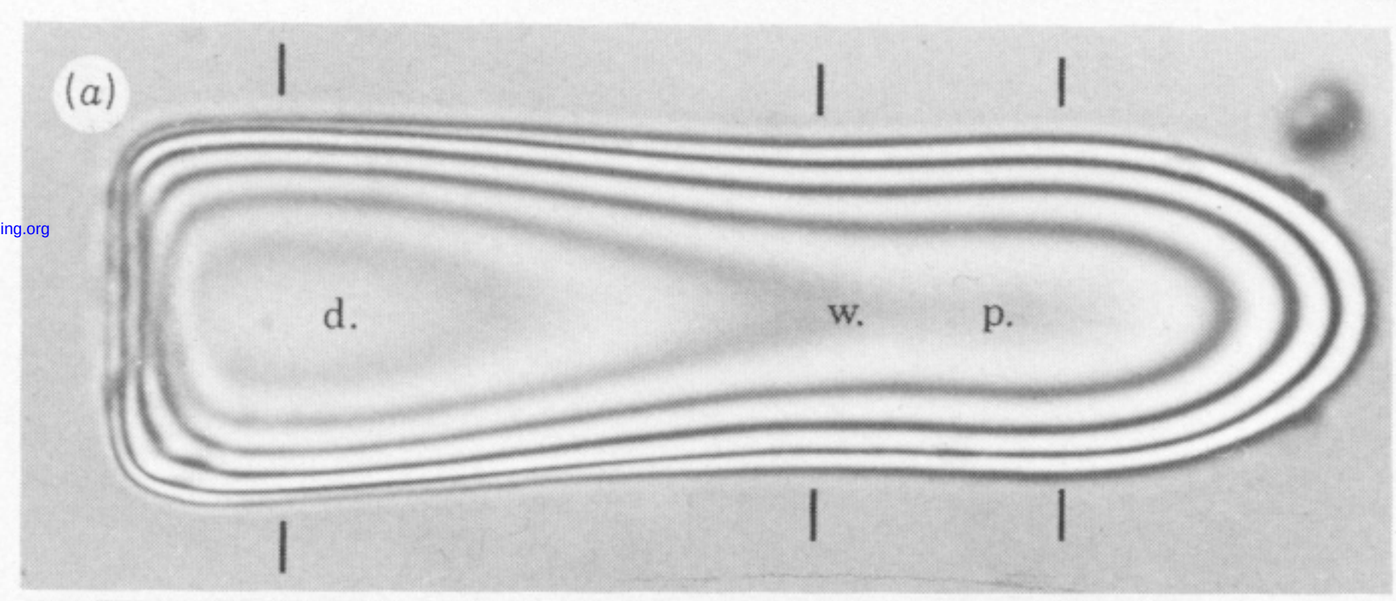

PHILOSOPHICAL TRANSACTIONS OF THE ROYAL SOCIETY B BIOLOGICAL SCIENCES

FIGURES 9 AND 11. For description see opposite.